

1 **A quantitative principle to understand 3D cellular connectivity in**  
2 **epithelial tubes**

3

4 Pedro Gómez-Gálvez<sup>1,2,†</sup>, Pablo Vicente-Munuera<sup>1,2,†</sup>, Samira Anbari<sup>3,†</sup>,  
5 Antonio Tagua<sup>1,2,†</sup>, Carmen Gordillo-Vázquez<sup>1,2</sup>, Ana M. Palacios<sup>1,2</sup>, Antonio  
6 Velasco<sup>1</sup>, Carlos Capitán-Agudo<sup>1</sup>, Clara Grima<sup>5</sup>, Valentina Annese<sup>1,2</sup>, Rafael  
7 Robles<sup>5</sup>, Alberto Márquez<sup>5</sup>, Javier Buceta<sup>3,4,\*</sup>, Luis M. Escudero<sup>1,2,\*</sup>

8

9 1: Instituto de Biomedicina de Sevilla (IBiS), Hospital Universitario Virgen del  
10 Rocío/CSIC/Universidad de Sevilla and Departamento de Biología Celular,  
11 Universidad de Sevilla. 41013 Seville, Spain.

12 2: Biomedical Network Research Centre on Neurodegenerative Diseases  
13 (CIBERNED), Madrid, Spain.

14 3: Chemical and Biomolecular Engineering Department, Lehigh University.  
15 Bethlehem, PA 18018, USA.

16 4: Bioengineering Department, Lehigh University. Bethlehem, PA 18018,  
17 USA.

18 5: Departamento de Matemática Aplicada I, Universidad de Sevilla. 41012  
19 Seville, Spain.

20

21

22 †: These authors contributed equally to this work.

23 \*: Corresponding authors

24

1 **ABSTRACT**

2 Apico-basal cell intercalations (scutoids) optimize packing and energy  
3 expenditure in curved epithelia. Further consequences of this new paradigm of  
4 tissue packing remain uncharacterized. In particular, how scutoids modify the  
5 3D cellular connectivity is an open question. This property is crucial for  
6 understanding epithelial architecture and is instrumental for regulating the  
7 biological function of tissues. Here, we address this problem by means of a  
8 computational model of epithelial tubes and a biophysical approach that links  
9 geometrical descriptors with the energetic cost required to increase the cellular  
10 connectivity. Our results predict that epithelial tubes satisfy a novel  
11 quantitative principle: the “Flintstones’ law”. In short, cellular connectivity  
12 increases with tissue thickness/curvature in a logistic way. We confirm  
13 experimentally the existence of this principle using *Drosophila*’s salivary  
14 glands. Our study provides methodological advances to analyze tissue  
15 packing in 3D and, more importantly, unveils a morphogenetic principle with  
16 key biological consequences.

17 **KEYWORDS**

18 Epithelial architecture, Tubulogenesis, Mathematical/Biophysical modeling,  
19 Computational geometry, Developmental systems biology, Cellular  
20 connectivity.

21

22

## 1 INTRODUCTION

2 During the last decades much progress has been achieved in the  
3 understanding of the emergence of self-organization in tissues. This problem  
4 has been addressed from the viewpoint of energetics drivers (Alt *et al*, 2017;  
5 Nelson *et al*, 2005; Siedlik *et al*, 2017; Trepap *et al*, 2009; Misra *et al*, 2017;  
6 Sugimura *et al*, 2016; Fletcher *et al*, 2014; Canela-Xandri *et al*, 2011),  
7 material-like properties (Yang *et al*, 2017; Bi *et al*, 2015; Pérez-González *et al*,  
8 2019; Latorre *et al*, 2018; Mongera *et al*, 2018; Campàs *et al*, 2014), and the  
9 analysis of the packing properties. As for the latter, the analysis of epithelial  
10 surfaces as tessellations of convex polygons has been successfully used to  
11 quantitatively understand different biological aspects such as tissue patterning,  
12 cell division, and growth (Mao *et al*, 2013; Thompson, 1945; Farhadifar *et al*,  
13 2007; Gibson *et al*, 2011, 2006; Lewis, 1928; Honda, 1978; Sánchez-Gutiérrez  
14 *et al*, 2016; Curran *et al*, 2017). Importantly, these studies have also revealed  
15 the validity of mathematical principles with biological consequences. One  
16 relevant example are the implications of Euler's formula (Reinhardt, 1918;  
17 Wetzel, 1926) about cellular connectivity. This principle states that polygonal  
18 cells in packed tissues, on average, have six neighbors (i.e., the average 2D  
19 cellular connectivity reads  $\langle n_{2D} \rangle = 6$ ). As for its biological consequences, the  
20 degree of cellular connectivity determines, for example, the strength of the  
21 cell-cell juxtacrine signaling (Tung *et al*, 2012; Sharma *et al*, 2019; Perrimon  
22 *et al*, 2012). Not surprisingly, the validity of this connectivity principle to the  
23 third dimension has been taken for granted since the role played by apico-  
24 basal cell intercalations has been disregarded and cells have been assumed  
25 to have prismatic-like shapes in either planar or bended epithelia.

26 However, the recent discovery of more complex cellular geometries in  
27 epithelial cells, i.e., scutoids, to reach an efficient three-dimensional (3D)  
28 tissue packing has set a new paradigm that has not been yet fully explored  
29 (Mughal *et al*, 2018; Gómez-Gálvez *et al*, 2018; Rupprecht *et al*, 2017).  
30 Scutoids imply spatial changes in the neighboring relationship between cells  
31 (**Fig. 1a**). This phenomenon is then a spatial version of the T1 transitions that  
32 produce cell rearrangements with time in numerous developmental processes  
33 (Bertet *et al*, 2004; Spencer *et al*, 2017; Irvine & Wieschaus, 1994). Thus, the

1 presence of scutoids necessarily modifies the connectivity and the biophysical  
2 properties of tissues. Still, the analysis of tissue organization in a 3D context,  
3 and the corresponding biological repercussions, have been hindered by the  
4 technical difficulties to accurately segment and reconstruct cells from apical to  
5 basal surfaces. In addition, very few computational models account for the  
6 presence of apico-basal transitions to investigate 3D self-organization in  
7 tissues (Okuda *et al*, 2019; Mughal *et al*, 2018; Gómez-Gálvez *et al*, 2018;  
8 Rupprecht *et al*, 2017).

9 The realistic analysis of 3D packing is in turn utterly relevant in epithelial  
10 tubes, where scutoids appear more frequently (Sanchez-Corrales *et al*, 2018;  
11 Iruela-Arispe & Beitel, 2013; Gómez-Gálvez *et al*, 2018). Epithelial tubes are in  
12 fact the primary developmental structures in all organisms with bilateral  
13 symmetry (Gilbert & Barresi, 2016) and tubulogenesis is fundamental in a  
14 broad variety of key developmental processes, including gastrulation and  
15 neurulation (Pilot & Lecuit, 2005; Swanson & Beitel, 2006; Colas &  
16 Schoenwolf, 2001; Leptin & Grunewald, 1990; Nelson, 2009; Iruela-Arispe &  
17 Beitel, 2013). Furthermore, epithelial tubes are the essential functional unit of  
18 many mammalian organs, including glands, components of the digestive  
19 apparatus, lungs, and kidney (Huebner & Ewald, 2014). Hence, the faithful  
20 formation and function of tubes requires the precise coordination of dynamic  
21 changes in the tissue architecture, i.e., packing, during development (Röper,  
22 2018).

23 Here, we study the packing and the 3D cellular connectivity properties of  
24 epithelial tubes. We show that the presence of scutoids implies a breakdown  
25 of the principle  $\langle n_{3D} \rangle = 6$  and reveal a novel law that quantitatively links the 3D  
26 cellular connectivity, geometrical descriptors (e.g., tissue curvature/thickness),  
27 and energetics drivers. Our findings are supported by i) a computational model  
28 that realistically render the 3D cellular organization of tubular epithelia  
29 (including the appearance of scutoids); ii) a biophysical model, supported by  
30 mathematical calculations, that connects the tissue energetics with the 3D  
31 organization of epithelial tubes; and iii) experimental data of epithelial tubes  
32 (*Drosophila's* salivary gland) whose 3D cellular structure has been accurately  
33 characterized by means of a novel computer-aided image analysis method.

1 Altogether, by realistically capturing the organization of cells in tubular  
2 epithelia, we shed light on the important issue of how tissues are 3D shaped  
3 and we open the door to understand quantitatively key morphogenetic events  
4 that ultimately depends on the 3D cellular connectivity.

5

## 6 **RESULTS**

### 7 **A computational model unveils the connectivity properties of tubular** 8 **epithelia**

9 To understand how the geometry of tubular epithelia affects the 3D cellular  
10 packing and connectivity, we designed and implemented a computational  
11 Voronoi tubular model (Gómez-Gálvez *et al*, 2018) (**Materials and Methods**).  
12 We analyzed tubes with an increasing surface ratio (radial expansion),  
13  $s_b = R_b/R_a$  (**Fig. 1b**). This parameter quantifies the ratio of the non-trivial  
14 curvatures of apical and basal tubular surfaces,  $\kappa_a/\kappa_b = R_b/R_a = s_b$ , and it is  
15 a proxy for the dimensionless tissue thickness,  $(R_b - R_a)/R_a = (s_b - 1)$ . In  
16 addition, we explored the cellular organization of tubes by using a Centroidal  
17 Voronoi Tessellation (CVT) scale (**Fig. 1c**). The CVT scale accounts for the  
18 number of iterations of the homogenizing Lloyd's algorithm and makes  
19 possible to analyze the effect of the topological order of the tissue (**Materials**  
20 **and Methods**) (Sánchez-Gutiérrez *et al*, 2016; Gómez-Gálvez *et al*, 2018).

21 Our results showed that the average number of apico-basal intercalations  
22 per cell,  $\langle i(s_b) \rangle$ , (**Fig. 1d**), and therefore the percentage of cells adopting the  
23 scutoidal shape (**Fig. S1**), increases with  $s_b$  and decreases as tubes become  
24 more ordered (i.e., as the CVT index increases). To further uncover the 3D  
25 organization of tissues, we implemented a benchmark able to reveal  
26 simultaneously the existence of apico-basal intercalations (scutoids) and the  
27 polygonal distributions of cells. To that end, we computed the probability that  
28 cells change their polygonal class between the apical and basal surfaces.  
29 Thus, the components (i.e., bins) of this distribution along the diagonal  
30 account for prismatic cells (**Fig. 2a**) whereas the spreading away from the  
31 diagonal reveals the existence of scutoids (cells that exchange neighbors due  
32 to apico-basal intercalations) and, consequently, changes in the cellular 3D  
33 connectivity in the tissue (**Fig. 2b**). In agreement with the results shown in **Fig.**

1 **1d**, our data indicates that the degree of spreading of the distribution (as  
2 quantified by the parameter,  $\eta^2$ , **Materials and Methods**) increases with the  
3 surface ratio and decreases when the initial (i.e., apical) Voronoi diagram  
4 became more ordered, that is, as the CVT increases (**Fig. 2c**).

5 Moreover, we computed the average of the total number of contacts of the  
6 cells,  $\langle n_{3D} \rangle$ , as a function of the surface ratio and the initial Voronoi diagram  
7 (**Fig. 2d**). Our data are quantitatively consistent with a mathematical derivation  
8 that shows that  $\langle n_{3D} \rangle$  is linearly proportional to the amount of apico-basal  
9 intercalations (**Materials and Methods** and **Fig. S1**). Also, these results  
10 indicated that the average cellular connectivity grows as the tissue thickness  
11 and the randomness of cellular organization increases.

12 In summary, our computational model suggests a relation between the  
13 tissue geometry (i.e., cell thickness/curvature), the cellular planar topological  
14 order (CVT index), and the 3D cellular connectivity in epithelial tubes.

15

### 16 **The 3D neighbor's accumulation follows a “poor get richer” principle**

17 In order to shed light on the underlying mechanisms that determine the  
18 degree of 3D cellular connectivity in tubular epithelia, we computed the net  
19 gain of cellular neighbors as a function of the radial expansion  
20 (thickness/curvature of tubes) and the topological properties of cells (CVT  
21 index and polygonal class at the apical surface). As a general trend, we  
22 observed that, independently of the radial expansion, the smaller the number  
23 of neighbors at the apical surface the larger the net gain of 3D cellular  
24 contacts (**Fig. 3a-b, Fig. S2**). Additionally, we also checked that this tendency  
25 is satisfied when estimating the net gain of neighbors accumulated from the  
26 basal to the apical surface (**Fig. S2**). These results suggest that in tubular  
27 epithelia the 3D cell packing follows a “poor get richer” principle driven by  
28 apico-basal intercalations: the less neighbors a cell has in a surface (apical or  
29 basal), the larger the net increase of cellular contacts. Interestingly, this result  
30 is akin to the behavior found in planar geometries that indicates that the  
31 probability of undergoing a T1 transition increases as the number of neighbors  
32 decreases (Bi *et al*, 2014), see Discussion.

1

2 **An energetics model suggests that cellular connectivity satisfies a**  
3 **logistic-like law**

4 In light of this evidence, and in order to better understand the dependence  
5 of the tissue self-organization on the radial expansion,  $s = R/R_a$ , we  
6 developed a biophysical model (a Kolmogorov rate equation) that accounts for  
7 the probability of cells to increase their 3D connectivity driven by energetic  
8 cues (**Fig. 4a-b** and **Materials and Methods**):

9 
$$\frac{dP_m(s)}{ds} = P_{m-1}(s)r_{m-1,m} - P_m(s)r_{m,m+1} \quad (1)$$

10 where,  $P_m$ , is the probability of having  $m$  accumulated 3D neighbors (i.e.,  
11  $m = n_{3D}$ ) as the surface ratio (i.e., tissue thickness) changes from  $s$  to  $s + ds$ ,  
12 and  $r_{i,i+1}$  accounts for the rate per unit of surface ratio of undergoing an apico-  
13 basal intercalation. By drawing parallels between apico-basal intercalations  
14 and planar T1 transitions (Sanchez-Corrales *et al*, 2018; Gómez-Gálvez *et al*,  
15 2018) we assumed that cells need to overcome an energy barrier to gain a 3D  
16 neighbor, that is,  $r_{i,i+1} \sim e^{-\Delta E_i}$  (**Fig. 4a-b**). The “poor get richer” principle  
17 suggests that  $\Delta E_i$  grows as  $i$  increases. In addition, our mathematical  
18 calculations proved that the apico-basal intercalation rate becomes null for a  
19 finite value of  $i$  (**Box** and **Materials and Methods**): neighbors’ gaining is  
20 necessarily bounded or, energetically speaking, the energy barrier to undergo  
21 an apico-basal transition becomes eventually infinite. All these facts led to the  
22 following expression for the apico-basal intercalation rate:  $r_{i,i+1} = \alpha(N_{max} -$   
23  $i)e^{-i\beta}$ , where  $\alpha$  is a ‘bare’ transition rate,  $\beta$  is the dimensionless energy (in  
24 units of the four-fold vertex energy configuration) per 3D neighbor that a cell  
25 needs to increase its connectivity to an additional cell, and  $N_{max}$  is the  
26 maximum 3D cellular connectivity (**Materials and Methods**).

27 The fitting of the *in silico* data about the average tissue connectivity,  
28  $\langle n_{3D}(s) \rangle = \sum_m m P_m(s)$ , to this biophysical model showed an excellent  
29 agreement and confirmed that  $\langle n_{3D} \rangle > 6$  as long as the tissue is subjected to  
30 some level of anisotropic curvature (**Fig. 4c**, **Fig. S3** and **Materials and**  
31 **Methods**). We also observed that the energy required per 3D neighbor to  
32 undergo an intercalation,  $\beta$ , quickly reached a plateau,  $\beta \simeq 5 \cdot 10^{-2}$ , as the



1 tissue became more ordered (i.e., as the CVT index increases). Our results  
2 also indicate that in Voronoi tubes the scutoidal geometry enables a  
3 theoretically increase of the average 3D cellular connectivity up to  
4  $\langle N_{max} \rangle \sim 12 - 15$  cells (**Table S1**). In addition, the plausibility of the Kolmogorov  
5 approach was further assessed by predicting the 3D neighbor distribution,  
6  $P_m(s)$ , thus confirming that a link between geometrical and energetic traits  
7 determines the cellular connectivity in tubular epithelia (**Fig. 4c**).

8 We also obtained theoretically an analytical formula that characterizes the  
9 average 3D cellular connectivity,  $\langle n_{3D} \rangle$  (**Box and Materials and Methods**).  
10 We concluded that in tubular epithelia  $\langle n_{3D} \rangle$  can be described by a logistic-like  
11 behavior,

$$12 \quad \langle n_{3D}(s) \rangle \approx \langle N_{max} \rangle \frac{1 + b e^{-\frac{s}{c}}}{1 + d e^{-\frac{s}{c}}} \quad (2)$$

13 where  $b$ ,  $c$ , and  $d$  are non-independent parameters that are functions of  $\alpha$ ,  $\beta$ ,  
14 and  $\langle N_{max} \rangle$  (**Table S1 and Materials and Methods**). We refer to this logistic-  
15 like principle as the “Flintstones’ law” after the cartoon characters.

16 The analysis of computational tubes revealed the validity of the Flintstones’  
17 law as an effective way to determine the cellular connectivity in tubular  
18 epithelia as a function of the radial expansion (**Fig. 4c and Fig. S3**). More  
19 importantly, it provides a straightforward way to estimate/predict the value of  
20 the underlying energetic properties regulating apico-basal intercalations and  
21 the limiting average 3D cellular connectivity (**Table S1**).

22

### 23 **Experiments confirm that the 3D cellular connectivity in tubular epithelia** 24 **satisfies the Flintstones’ law**

25 In order to confirm our computational and theoretical predictions, we  
26 implemented a novel methodological pipeline that combines several  
27 computational image analysis techniques to accurately segment cells of *in vivo*  
28 epithelial tubes (Arganda-Carreras *et al*, 2017; Machado *et al*, 2019)  
29 (**Materials and Methods**). We used the *Drosophila* larval salivary gland as a  
30 model due to its ideal characteristics to study complex tubular architectures  
31 (Girdler & Röper, 2014) (**Fig. 5a-c**).



1 Our methodology allowed to determine the average surface ratio of the  
2 salivary glands ( $s_b = 4.0 \pm 0.4$ ),  $\langle n_{3D}(s_b) \rangle = 6.7 \pm 0.2$ , the average percentage  
3 of scutoids ( $76 \pm 11\%$ ), and the average number of apico-basal intercalations  
4 per cell,  $\langle i(s_b) \rangle = 1.4 \pm 0.4$ , thus confirming the validity of the formula that  
5 relates apico-basal intercalations per cell and the average connectivity:  
6  $\langle n_{3D} \rangle = 6 + \langle i \rangle / 2$  (**Materials and Methods** and **Fig. S1**). We also calculated  
7 the polygonal class distribution in the apical and basal surfaces (**Fig. S4**).  
8 Interestingly, in spite of the prevalence of scutoids, the polygonal organization  
9 of apical and basal surfaces was found to be the same and equivalent to that  
10 obtained in *in silico* V8 tubes with a radial expansion  $s_b = 1.75$  (**Fig. S4**). This  
11 V8 model ( $s_b = 1.75$ ) also displayed a similar scutoidal prevalence ( $79 \pm 5\%$ ),  
12 average number of 3D neighbors, average number of apico-basal  
13 intercalations per cell, and  $\eta^2$  spreading that *in vivo* tubes (**Fig. 5d** and **Fig.**  
14 **S4**). We additionally confirmed that the apical and basal surfaces of the V8  
15 model and the salivary glands fulfilled, as expected, that  $\langle n_{2D} \rangle \approx 6$  (Reinhardt,  
16 1918; Wetzel, 1926) (**Fig. S4**). Thus, we concluded that the *in silico* V8 model  
17 with a radial expansion of  $s_b = 1.75$  faithfully recapitulates the 3D packing  
18 properties of *in vivo* salivary glands.

19 As for the 3D cellular connectivity of *in vivo* tubes, our analyses confirmed  
20 that the “poor get richer” principle was satisfied, thus supporting the idea that  
21 the smaller the number of neighbors of a cell in a surface, the larger the  
22 probability to increase its connectivity (**Fig. S4**). Additionally, by implementing  
23 an un-rolling (i.e., peel-off) algorithm (Yang *et al*, 2019) (**Materials and**  
24 **Methods**), we obtained concentric radial sections and quantified the number  
25 of 3D neighbors as a function of the radial expansion. The fitting of the data to  
26 the Kolmogorov model showed an excellent agreement and allowed to  
27 estimate the energetic properties as summarized by the parameter  $\beta$  (**Fig. 5e**  
28 and **Table S1**). Our results suggested that the energy per 3D cell required to  
29 undergo an apico-basal intercalation is larger in *in vivo* tubes than in the  
30 computational V8 model, see Discussion. Importantly, the 3D cellular  
31 connectivity data confirmed the applicability of the Flintstones’ law in *in vivo*  
32 tubular epithelia (**Fig. 5e** and **Table S1**).

33

## 1 DISCUSSION

2 Here we have shown how mathematical and physical principles underlie the  
3 emergence of functionally complex 3D developmental structures, e.g., glands.  
4 Our analyses have uncovered for the first time how a 2D organizational trait,  
5 i.e., the cellular connectivity, can be extended to the third spatial dimension  
6 when the novel paradigm of epithelial cells' shapes and packing, the scutoid,  
7 is considered. In that regard, we have revealed how the 3D cellular  
8 connectivity and tissue energetics are coupled, and we have stated a novel  
9 principle, the so-called Flintstones' law. The latter links the activation energy  
10 needed to recruit additional neighbors with geometrical descriptors (i.e., tissue  
11 thickness/curvature). Our results provide new biological insight into the  
12 spatiotemporal regulation of cell-cell connectivity, a property that ultimately  
13 regulates juxtacrine signaling and is pivotal for primordia patterning and cell  
14 fate determination (Tung *et al*, 2012; Sharma *et al*, 2019). In this context, our  
15 study points towards an effect of scutoids on the regulation of the physiological  
16 properties of tissues. Therefore, our findings, on top of being fundamental to  
17 understand self-organization of epithelia in 3D, open new ways to investigate,  
18 and draw implications about, primary developmental processes in which  
19 epithelial bending is essential such as tubulogenesis, gastrulation, or  
20 neurulation.

21 Our study also provides important methodological advances. Previous  
22 software developed to identify the outlines of the epithelial cells does not work  
23 on 3D or lacks enough precision to extract the geometrical and topological  
24 data needed to quantify tissue packing in 3D (Khan *et al*, 2014; Heller *et al*,  
25 2016; Bassel *et al*, 2014; Gómez-Gálvez *et al*, 2018). Here we have shown  
26 that our methodological pipeline (**Materials and Methods**) allows to  
27 implement a 3D segmentation and the precise reconstruction of cells in  
28 epithelia subjected to curvature. We stress that this level of detail is necessary  
29 to be able to quantify the apico-basal intercalation phenomenon and,  
30 therefore, compare the results with the computational models and extract  
31 biological consequences. We then argue that our methodology, by enabling  
32 the analysis of 3D packing in a realistic way, will benefit the field of  
33 morphogenesis by bringing understanding about the cellular and mechanical

1 basis of self-organization in curved tissues (Inoue *et al*, 2019; Ambrosini *et al*,  
2 2017; Hirashima & Adachi, 2019) or even whole embryos (Shahbazi *et al*,  
3 2019). In addition, our analysis indicates that the Flintstones' law can be used  
4 quantitatively to estimate key connectivity-related parameters, e.g.,  $\beta$  and/or  
5  $\langle N_{max} \rangle$ . This avoids the burden of solving the optimization problem associated  
6 with the Kolmogorov model that is computationally demanding (**Material and**  
7 **Methods**). Thus, the values obtained by means of fittings to the Flintstones'  
8 law are, at the very least, within the same order of magnitude with respect to  
9 the 'exact' Kolmogorov calculations (**Table S1**). This reveals the usability of  
10 the Flintstones' law not just as a principle that is satisfied by tubular epithelia,  
11 but as a practical way to connect packing properties, geometrical descriptors,  
12 and biophysical traits due to its predictive character.

13 As a matter of discussion, the connectivity law that we have introduced  
14 herein, depends on a prediction obtained from the Voronoi computational  
15 model that was confirmed in experiments: the "poor get richer" principle.  
16 Roughly speaking, we have shown that the fewer neighbors a cell has on a  
17 surface, the larger is the probability of a connectivity increase. Interestingly, a  
18 similar idea has been reported in T1 dynamical processes during the  
19 remodeling of planar epithelia (Bi *et al*, 2014). Since the scutoidal geometry  
20 can be related to planar T1 transitions by exchanging the concepts of space  
21 and time, this result reinforces the idea of the existence of universal principles  
22 driving the organization of tissues.

23 In our study we have found that in real tissues the energy cost per 3D  
24 neighbor that a cell requires to increase its connectivity,  $\beta$ , is larger than in  
25 Voronoi models. We hypothesize that it is due to the purely geometrical  
26 description used in the latter. That is, while in *in silico* models the apico-basal  
27 transitions develop just a result of a topological constraint (Voronoi  
28 tessellation), in the salivary glands, on top of geometrical requirements, the  
29 cells must actively remodel their cytoskeleton to make the transitions possible.  
30 That component would explain the larger effective cost of gaining new  
31 neighbors in real tissues. The reduced energetic cost for gaining neighbors in  
32 the Voronoi computational approach also explains why *in silico* tubes led to a  
33 larger limiting average 3D cellular connectivity,  $\langle N_{max} \rangle$ , and the V8 model with

1 the same surface ratio that the salivary gland,  $s_b = 4$ , developed more apico-  
2 basal transitions than the real samples (**Fig. 5e**, **Fig. S4**, and **Table S1**).  
3 These data ultimately explain why it is necessary to rescale appropriately  $s_b$  to  
4 obtain a computational model with packing, topological, and connectivity  
5 properties similar to those of the salivary glands. In that regard, our results  
6 suggest that salivary glands are optimized to reach a high cellular connectivity.  
7 While the *in silico* V8 model with a radial expansion of  $s_b = 1.75$  or  $s_b = 4$  are  
8 far from reaching their maximum average connectivity (i.e.,  $\langle n_{3D} \rangle$ 's are,  
9 respectively,  $\sim 47\%$  and  $\sim 61\%$  of  $\langle N_{max} \rangle$ ), in the salivary glands  $\langle n_{3D}(s_b) \rangle$  is  
10  $\sim 87\%$  of  $\langle N_{max} \rangle$  (**Fig. 5e**, **Fig. S4**, and **Table S1**). This optimization could be  
11 related to a functionality improvement of the gland, similarly to what has been  
12 suggested in pituitary growth hormone secretory cells, where the increase of  
13 3D cellular connectivity has been proposed to better coordinate the pulses of  
14 hormone secretion (Bonnefont *et al*, 2005).

15 As for the broader implications of our findings, we argue that, while our  
16 analyses focus on static tissues from the point of view of tissue architecture,  
17 our results can also be relevant to understand active 3D tissue remodeling  
18 (e.g., fluidization). Recent studies have revealed that active remodeling  
19 involves changes in the material-like properties of tissues that can be  
20 connected to an increased activity of neighbor exchanges (Tetley *et al*, 2019;  
21 Mongera *et al*, 2018). In that regard, here we have shown that the physical  
22 basis of 3D self-organization (i.e., 3D cellular packing and connectivity) in  
23 tubular epithelia effectively relies on a constant amount of energy,  $\beta$ . Thus,  
24 arguably, active 3D tissue remodeling would imply dynamical changes on the  
25 value of  $\beta$  that would modify the apico-basal intercalation propensity and  
26 therefore the material-like properties: the larger  $\beta$  the more solid-like the tissue  
27 would behave. Finally, with respect to the applicability of our results to other  
28 areas, we expect that the emerging field of organoids will benefit from our  
29 discoveries. A precise quantification of 3D connectivity could then help to  
30 understand the lack of reproducibility in organoid production, one of the  
31 biggest challenges of the field (Schutgens *et al*, 2019; Huch *et al*, 2017;  
32 Clevers, 2016). Also, from a medical point of view, it has been recently shown  
33 that tissue curvature affects tumor progression due to the imbalance of

1 tensions in apical and basal surfaces of epithelial tubes (Messal *et al*, 2019).  
2 The Flintstones' law explains how energetic cues affect the 3D packing of  
3 these cells and therefore may shed light on the mechanism of tumorigenic  
4 morphogenesis in tubular organs.

## 5 **MATERIALS AND METHODS**

### 6 **Immunohistochemistry and confocal imaging of salivary glands**

7 Flies were grown at 25 °C using standard culture techniques. We dissected  
8 the salivary glands from third instar larvae of the wild type *Oregon R* strain.  
9 After PBS dissection, the glands were fixed using 4% paraformaldehyde in  
10 PBS for 20 min. The samples were washed three times for 10 min with PBT  
11 (PBS, 0.3% Triton) and then incubated for 1 hr 45 minutes at room  
12 temperature with Cy3-labeled phalloidin (Sigma) to label the cell contours of  
13 the epithelial cells. Stained larval salivary glands were mounted using  
14 Fluoromount-G (Southern Biotech). We used two pieces of double-sided  
15 adhesive tape (one on top of each other) as a spacer (Aldaz *et al*, 2013), so  
16 the salivary glands preserve their shape. Images were taken using a Nikon  
17 Eclipse Ti-E laser scanning confocal microscope. The images were captured  
18 using a ×20 dry objective and 2.5 μm steps between slices. The image stacks  
19 were exported as 1024 × 1024 pixels TIFF files.

### 20 **3D glands segmentation**

21 To segment the salivary gland stacks of images and reconstruct (semi-  
22 automatically) the shape of cells in three dimensions we used the FIJI  
23 (Schindelin *et al*, 2012) plugin LimeSeg (Machado *et al*, 2019). We inferred  
24 cell outlines by using surface elements ("Surfels") obtained by placing single  
25 ellipsoidal-like seeds on every cell (see <https://imagej.net/LimeSeg> for details).  
26 Once cell outlines were found (**Fig. 5b-c**), we exported them as point clouds  
27 (output). We developed a custom-made Matlab code (2018a MathWorks) to  
28 postprocess the output of LimeSeg in order to correct errors and obtain  
29 perfectly segmented salivary glands. In addition, we manually segmented the  
30 lumen of the glands from the images using Adobe Photoshop CS6 and  
31 reconstructed it using a Matlab code. To faithfully represent the gland as a  
32 cylinder, we selected a subset of cells: cells that were not ductal, neither

1 located at the tip of the gland. For more information about the processing  
2 pipeline: <https://osf.io/nd5t6/>.

3 To obtain the cellular neighborhood relations of salivary glands for different  
4 values of the radial expansion, we proceeded as follows. We calculated the  
5 cell height by estimating the distance between the average voxel positions of  
6 the apical surface with respect to the average voxel positions of its basal  
7 surface,  $d(s_a, s_b)$ . Then, to capture a concentric radial section of the gland, we  
8 linearly extrapolated the equivalent cell height to the given surface ratio,  $s$ :

$$9 \quad d(s_a, s) = d(s_a, s_b) \frac{s}{s_b} \quad (3)$$

10 where  $d(s_a, s)$  is the Euclidean distance between the position of the centroid of  
11 the cell in apical and that the position of the centroid at a value  $s$  of the radial  
12 expansion. Finally, to obtain the gland cylindrical radial section for a given  
13 value of the radial expansion,  $s$ , we collected all voxels between apical and the  
14 upper bound of the calculated distance  $d(s_a, s)$ . Those cylindrical surfaces of  
15 the salivary gland were mapped in the Cartesian plane for analysis using a  
16 cylindrical coordinates transformation.

### 17 **Salivary glands measurements**

18 We quantified the following geometrical and topological descriptors of the  
19 segmented salivary glands using a custom-made Matlab code:

- 20 - Surface ratio expansion ( $s$ ): Assuming a cylindrical shape for glands,  
21 we estimated  $s$  by dividing the area of the basal surface of glands by  
22 area of the apical surface.
- 23 - Polygonal Class. We estimated the number of sides of each cell using  
24 the unrolled images (radial cylindrical sections) projected in the  
25 Cartesian plane.

26 Likewise, we carried out the calculations of the percentage of scutoids and  
27 the number of apico-basal transitions.

### 28 **Voronoi tubular model**

29 Using custom-made Matlab code (R2018a) we generated a Voronoi model  
30 that simulates the surface of a cylinder unfolded over the Cartesian plane, see  
31 details in Gomez-Galvez et al. ((Gómez-Gálvez *et al*, 2018), **Material and**

1 **Methods**). The only difference with the cited methodology, is that in this work  
2 the Voronoi diagrams has been constructed by means of the Delaunay  
3 triangulation technique. Therefore, we just considered the cells' vertices  
4 information (cartesian coordinates and connections) for a much faster  
5 computation. For each realization, we used an initial set of 200 randomly  
6 located seeds on a rectangular domain of 512 (X axis; transverse axis of  
7 cylinder) per 4096 (Y axis; longitudinal axis of cylinder). In total, we  
8 implemented 20 different realizations (i.e., tubes). We performed this  
9 procedure for 10 different initial Voronoi diagrams (Voronoi 1 (V1, random  
10 seeds) to Voronoi 10 (V10, more ordered and homogeneous cells). These  
11 diagrams represent the apical (inner) surfaces of computational tubes, and  
12 they were obtained by applying N-1 times the Lloyd's algorithm (Lloyd, 1982)  
13 to the random seeds, where N is then the resulting Voronoi model. For  
14 instance, to compute a V1, we use purely random seeds, while to obtain a V4  
15 diagram, it would be required to apply 3 times the Lloyd's algorithm to random  
16 seeds. V8 diagrams provide a polygonal organization in apical surfaces as  
17 experimentally observed (Main Text and **Fig. S4**). Subsequent radial sections  
18 that define computational tubes with different surface ratios were obtained by  
19 implementing a radial projection of the Voronoi seeds. For each apical surface  
20 of the tube, we generated 40 expansions by incrementing the surface ratios  
21 ( $s_b$ ) using 0.25 steps: 1 (apical), 1.25, 1.5, ... ,10 (maximum basal surface).

22 As for the 3D reconstruction of cells in Voronoi tubes, each set of seeds that  
23 characterizes cells on a given cylindrical section defines a unique 2D Voronoi  
24 diagram at every surface and hence the corresponding 2D cellular domains.  
25 The set of 2D Voronoi regions that belong to the same radially projected seed  
26 from the apical to the basal surface then define each 3D cellular shape. Each  
27 of the obtained 3D Voronoi cells was further processed using the Matlab  
28 function '*alphaShape*' to transform the set of voxels into a compact, solid,  
29 object. This reconstruction pipeline was implemented using Matlab (2018a).  
30 Code available at <https://osf.io/nd5t6/>.

### 31 **Voronoi tubular model measurements.**

32 We measured the following properties of cells in Voronoi tubular models:  
33 number of sides of cells for a given radial section, and total number neighbors.



1 Additionally, we computed the percentage of scutoids, the number of apico-  
 2 basal transitions, the polygon distribution of every surface (radial sections). In  
 3 these quantifications, we disregarded cells at the boundaries (tips of tubes) to  
 4 avoid ‘border effects’.

### 5 **In Voronoi tubes the net gain of 3D neighbors is bounded**

6 Assuming a cylindrical geometry (e.g., epithelial tubes), each point at a given  
 7 radial surface can be represented into the Cartesian plane; where coordinate  $x$   
 8 accounts for the cylindrical transversal coordinate and coordinate  $y$  for the  
 9 longitudinal one (see **Box**). Thus, if the coordinates of a point (e.g., a Voronoi  
 10 seed) at the apical surface are given by  $(x, y)$ , the coordinates of that point at  
 11 a surface with a value of the cylindrical radial expansion  $s \in [1, \infty)$  can be  
 12 found by defining the function  $f_s: \mathbb{R}^2 \rightarrow \mathbb{R}^2$   $f_s(x, y) = (sx, y)$ . Under these  
 13 conditions, we aim to characterize the seeds that generate scutoids  
 14 (exchanges in the neighboring relations of seeds) as  $s$  changes.

15 *Lemma 1.* Given three non-collinear points  $\{A, B, C\}$  that define a circle (a  
 16 nearest-neighbors relation), and another exterior point  $D$ , if  $s > 1$  exists such  
 17 that  $f_s(D)$  is interior to the circle defined by  $\{f_s(A), f_s(B), f_s(C)\}$ , then  $D$  is inside  
 18 of the vertical parabola containing  $\{A, B, C\}$  (**Box**).

19 *Remark.* If two of the three points  $\{A, B, C\}$  are on the same vertical line, then  
 20 the parabola considered in Lemma 1 degenerates as a vertical strip. Even in  
 21 this case, the thesis of the Lemma is true if we replace the interior of the  
 22 parabola by the inside of the strip.

23 *Proof.* Without loss of generality, we can suppose that  $\{A, B, C\}$  are  
 24 counterclockwise oriented. Thus, the point  $D(x, y)$  is outside the circle defined  
 25 by  $\{A, B, C\}$  if, and only if, the sign of the following determinant is negative:

$$26 \quad \begin{vmatrix} a_1 & a_2 & a_1^2 + a_2^2 & 1 \\ b_1 & b_2 & b_1^2 + b_2^2 & 1 \\ c_1 & c_2 & c_1^2 + c_2^2 & 1 \\ x & y & x^2 + y^2 & 1 \end{vmatrix} = \begin{vmatrix} a_1 & a_2 & a_1^2 & 1 \\ b_1 & b_2 & b_1^2 & 1 \\ c_1 & c_2 & c_1^2 & 1 \\ x & y & x^2 & 1 \end{vmatrix} + \begin{vmatrix} a_1 & a_2 & a_2^2 & 1 \\ b_1 & b_2 & b_2^2 & 1 \\ c_1 & c_2 & c_2^2 & 1 \\ x & y & y^2 & 1 \end{vmatrix} < 0 \quad (4)$$

27 For the sake of simplicity, we represent the previous equation as:

$$28 \quad \det(\mathcal{A}) = \det(\mathcal{B}) + \det(\mathcal{C}) < 0 \quad (5)$$

1 On the other hand, by considering  $x$  and  $y$  as variables, the equation  
 2  $\det(\mathcal{A}) = 0$  corresponds to the circle defined by  $\{A, B, C\}$ , and  $\det(\mathcal{B}) = 0$   
 3 corresponds to the vertical parabola defined by the same three points.  
 4 Consequently, the inequality  $\det(\mathcal{B}) > 0$  defines the locus of interior points to  
 5 that parabola.

6 Now, assuming that  $s > 1$  exists such that  $f_s(D)$  is interior to the circle  
 7 defined by  $\{f_s(A), f_s(B), f_s(C)\}$ . Then,

$$\begin{vmatrix} sa_1 & a_2 & s^2a_1^2 + a_2^2 & 1 \\ sb_1 & b_2 & s^2b_1^2 + b_2^2 & 1 \\ sc_1 & c_2 & s^2c_1^2 + c_2^2 & 1 \\ sx & y & s^2x^2 + y^2 & 1 \end{vmatrix} = s^3 \det(\mathcal{B}) + s \det(\mathcal{C}) > 0 \quad (6)$$

8 Or, equivalently,  $s^2 \det(\mathcal{B}) + \det(\mathcal{C}) > 0$ , so,  $s^2 \det(\mathcal{B}) > -\det(\mathcal{C})$ . If  
 9  $\det(\mathcal{B}) < 0$ , then  $1 < s^2 < -\frac{\det(\mathcal{C})}{\det(\mathcal{B})}$  and therefore  $\det(\mathcal{B}) > -\det(\mathcal{C})$ . The latter  
 10 is in contradiction with  $\det(\mathcal{B}) + \det(\mathcal{C}) < 0$ . As a result,  $\det(\mathcal{B}) > 0$ , and the  
 11 following inequality holds,

$$s^2 > -\frac{\det(\mathcal{C})}{\det(\mathcal{B})} > 1 \quad (7)$$

12 Notice that if the circle defined by  $\{A, B, C\}$  is surrounded by a set of points  
 13 and we change continuously the parameter  $s$  in the interval  $[1, \infty)$ , it is  
 14 possible to detect the first point touching the circle defined by  
 15  $\{f_s(A), f_s(B), f_s(C)\}$ . That point can be obtained by computing all the points at  
 16  $s = \sqrt{-\frac{\det(\mathcal{C})}{\det(\mathcal{B})}}$ . Hence, the first point contacting the circle will be that with the  
 17 minimum value of  $s$ .

18 As for proving that the average of the number of neighbours of a cell induced  
 19 by a seed grows is bounded as a function of the surface ratio, we state the  
 20 following proposition:

21 *Proposition 1.* Given a Voronoi seed representing a cell, if  $n_{3D}(s)$  is the total  
 22 number of accumulated cell neighbors as  $s$  increases from  $s = 1$  (apical  
 23 surface) to a given value of  $s$ , then  $\langle n_{3D}(s) \rangle$  is a bounded function for a finite  
 24 cylinder.

25

1 *Proof.* We model the apical surface as the cylinder  $2\pi r \times h$ , where  $r$   
 2 represents the inner radius and  $h$  the length of the cylinder. Given a seed  $A$   
 3 in that surface, in the corresponding Delaunay triangulation it appears as a  
 4 point surrounded by triangles defining the neighbourhood of  $A$ . By Lemma 1,  
 5 each triangle defines a vertical parabola and a circle. So, any other seed  
 6 touching  $A$  in other layer must be inside of one of the parabolas and outside of  
 7 all circles (see **Box**). Let's denote  $\mathcal{R}_{s,A}$  the feasible region for a new neighbour  
 8 of  $A$  in the layer represented by  $s$ , i.e., all points inside one of the parabolas  
 9 and outside all the circles. Thus, if  $\#(\mathcal{R}_{s,A})$  is the number of seeds in that  
 10 region that are not neighbours of  $A$  in the apical surface, obviously, an upper  
 11 bound to the number of new neighbours to  $A$  is given by  $\#(\mathcal{R}_{s,A}) \leq \#(\mathcal{R}_{1,A})$ .

12

13 On the other hand, that number of seeds is, in average, proportional to the  
 14 density of seeds times the area of  $\mathcal{R}_{s,A}$ , therefore, the average number of  
 15 accumulated neighbours of  $A$ , denoted as  $\langle n_{3D}(A) \rangle$ , will be bounded by the  
 16 change of the density of points when growing  $s$ , this is to say,

17

$$18 \quad d\langle n_{3D}(A) \rangle \leq M \cdot \frac{\mathcal{R}_{s,A}}{2\pi sr \cdot h} ds \quad (8)$$

19

20 where  $M$  represents the total number of seeds (i.e., the total number of cells  
 21 that is a constant) and the quotient is the area of  $\mathcal{R}_{s,A}$  divided by the area of a  
 22 given radial layer. In general, it is not possible to integrate equation (4), since  
 23 the area of  $\mathcal{R}_{s,A}$  is known only in very few, particular, cases.

24

25 If the case of a finite cylinder,  $\langle n_{3D}(A) \rangle \leq \#(\mathcal{R}_{s,A}) \leq \#(\mathcal{R}_{1,A})$  leads, suming up  
 26 to all the seeds and dividing by  $M$ , to the upper bound

27

$$28 \quad \langle n_{3D}(s) \rangle \leq \frac{1}{M} \cdot \sum_A \#(\mathcal{R}_{1,A}) \quad (9)$$

29

30 thus,  $\langle n_{3D}(s) \rangle$  is necessarily a bounded function. This expression indicates  
 31 that the number of new neighbours when increasing  $s$  exhausts since the  
 32 number of cells is a resource shared by all the layers. It is possible to obtain

1 an upper bound to  $\langle N_{max} \rangle = \lim_{s \rightarrow \infty} \langle n_{3D}(s) \rangle$  since, after a flip in the Delaunay  
 2 triangulation, the edge disappearing (i.e., a cell contact loss) can never be  
 3 recovered in a cylindrical geometry. Thus,  $M \cdot (\langle N_{max} \rangle - n_{3D}(1))$  is bounded  
 4 by the number of edges that complement the original Delaunay triangulation  
 5 on the apical surface, that is,

$$7 \quad \langle N_{max} \rangle - \langle n_{3D}(1) \rangle \leq \frac{1}{M} \cdot \left( \frac{M(M-1)}{2} - M \frac{\langle n_{3D}(1) \rangle}{2} \right) = \frac{M-1}{2} - \frac{\langle n_{3D}(1) \rangle}{2} \quad (10)$$

8 leading to

$$9 \quad \langle N_{max} \rangle \leq \frac{M-1}{2} + \frac{\langle n_{3D}(1) \rangle}{2} \leq \frac{M-1}{2} + 3 = \frac{M+5}{2} \quad (11)$$

10 Where we have assumed that  $\langle n_{3D}(1) \rangle = 6$ . The simulations of the  
 11 computational Voronoi model and the data of the salivary gland show that  
 12  $\langle N_{max} \rangle$  is in fact much smaller than the theoretical bound  $\frac{M+5}{2}$ .

13

#### 14 **Relation between total accumulated 3D neighbors and the number of** 15 **intercalation events**

16 Scutoids have a Euler characteristic  $\chi = 2$  such that  $V - E + F = 2$ , where  $V$ ,  
 17  $E$ , and  $F$  accounts for the number of vertexes, edges, and faces respectively.  
 18 We assumed that the apical,  $a$ , and basal,  $b$ , faces of scutoids tessellating a  
 19 cylindrical space have radial coordinates  $R_a$  and  $R_b$  respectively. Then, for any  
 20 value of the surface ratio expansion,  $s = R/R_a$ , these solids can be mapped  
 21 into a connected plane graph with the same Euler characteristic (a sort of  
 22 projection of the vertexes and connectors into the plane, see **Fig. S5**). Thus, as  
 23 a function of  $s$ , the accumulated number of 3D neighbors reads  $n_{3D}(s) =$   
 24  $E(s) - V(s)$ . Since in tubular geometries the centroids of tessellating scutoids  
 25 always separate from each other as  $s$  increases (i.e., apico-basal  
 26 intercalations are not reversible) for a single scutoid,

$$27 \quad n_{3D}(s) = \max(\{V(s)\}) = \min(\{V(s)\}) + i(s) \quad (12)$$

28 where  $\{V(s)\} = \{V(1), V(1 + ds), \dots, V(s_b)\}$  and  $i(s)$  denotes the number of  
 29 intercalation points in the interval  $s \in [1, s_b]$ . In the case of a 3D tessellation  
 30 with  $N$  cells, where  $M$  of them do not show any intercalation, the total number  
 31 of accumulated neighbors reads,

$$\begin{aligned}
 1 \quad n_{3D}(s) &= \sum_{j=1}^N n_{3D}^{(j)}(s) = \sum_{j=1}^M V^{(j)}(1) + \sum_{j=1}^{N-M} \max(\{V^{(j)}(s)\}) = \\
 2 \quad &\sum_{j=1}^M V^{(j)}(1) + \sum_{j=1}^{N-M} \{\min(\{V^{(j)}(s)\}) + i^{(j)}(s)\} \\
 3 \quad &(13)
 \end{aligned}$$

4 Given that each intercalation point is shared by four cells, two of them  
 5 necessarily increase their number of vertices in a given  $s$ -plane and two of  
 6 them decrease their number of vertices (see **Fig. 1a**). Thus, in the case of a  
 7 decrease  $\max(\{V^{(j)}(s)\}) = V^{(j)}(1)$  and in the case of an increase  
 8  $\min(\{V^{(j)}(s)\}) + i^{(j)}(s) = V^{(j)}(1) + i^{(j)}(s)$ . Consequently,

$$9 \quad n_{3D}(s) = \sum_{j=1}^N V^{(j)}(1) + \sum_{j=1}^{(N-M)/2} i^{(j)}(s) = \sum_{j=1}^N V^{(j)}(1) + \frac{1}{2} \sum_{j=1}^{N-M} i^{(j)}(s) \quad (14)$$

10 where we used the fact that for every intercalation event that increases by  
 11 one the number of neighbors there is one that decreases the number of  
 12 neighbors in the same amount; consequently, we can add up all intercalation  
 13 events and divide by two. Hence the average number of accumulated 3D  
 14 neighbors,  $\langle n_{3D}(s) \rangle = n_{3D}(s)/N$  reads  $\langle n_{3D}(s) \rangle = \langle V(1) \rangle + \langle i(s) \rangle / 2$ ;  $\langle i(s) \rangle$   
 15 being the average number of apico-basal intercalations per cell. Finally, by  
 16 considering that any  $s$ -surface, and in particular the apical surface  $s = 1$ ,  
 17 corresponds to a 2D tessellation of convex polygons,  $\langle V(1) \rangle = 6$  we conclude  
 18 that,

$$19 \quad \langle n_{3D}(s) \rangle = 6 + \frac{1}{2} \langle i(s) \rangle \quad (15)$$

20

## 21 **A Kolmogorov rate equation for the 3D cellular connectivity**

22 The probability,  $P$ , of having  $m$  accumulated 3D neighbors (i.e.,  $m = n_{3D}$ ) as  
 23 the surface ratio increases from  $s$  to  $s + ds$  can be described by the following  
 24 Markov equation (**Fig. 4b**),

$$25 \quad P_m(s + ds) = P_m(s)T_{m,m} + P_{m-1}(s)T_{m-1,m} \quad (16)$$

26 where  $T_{i,j}$  is the probability of incrementing the number of neighbors from  $i$  to  $j$   
 27 due to an apico-basal intercalation. Since  $\sum_j T_{i,j} = 1$  (normalization of the  
 28 transition probabilities) and  $T_{i,j} = f(i,j)\{\delta_{i-1,j} + \delta_{i,j+1}\}$  (each intercalation can  
 29 only possibly induce to win one neighbor) then  $T_{m,m} = 1 - T_{m,m+1}$  and the

1 above Markov equation can be written as a Kolmogorov equation (a.k.a.  
2 Master equation):

$$3 \quad \frac{dP_m(s)}{ds} = P_{m-1}(s)r_{m-1,m} - P_m(s)r_{m,m+1} \quad (17)$$

4 where  $r_{i,j}$  accounts for the probability of apico-basal intercalations per unit of  
5 surface ratio, i.e.,  $T_{i,j} = r_{i,j}ds$ .

6 If we assume an Arrhenius-like kinetics (Bi *et al*, 2014) then  $r_{i,i+1} = \hat{\alpha}e^{-\Delta E_i}$ ,  
7 where  $\hat{\alpha}$  is the so-called pre-exponential factor that modulates the “bare”  
8 frequency of intercalations (per unit of surface ratio expansion) and  $\Delta E_i$  is the  
9 activation energy in some energy units, e.g., in units of  $E_0$  (the value of the  
10 energetic barrier of the four-fold vertex configuration). The observed “poor get  
11 richer” behavior suggests that the activation energy,  $\Delta E_i$ , increases with  $i$ . For  
12 the sake of simplicity, up to first order in  $i$ :  $\Delta E_i = i \cdot \beta$  ( $\beta$  being the  
13 dimensionless activation energy of a cell per 3D neighbor in units of  $E_0$ ). On  
14 the other hand, the mathematical calculations (see Eq. (9)) indicate that the  
15 intercalation rate  $r_{i,i+1}$  becomes null for a finite value of  $i$  or, alternatively, that  
16 the activation energy becomes infinite for a finite value of  $i$ . Otherwise, the net  
17 gain of new neighbors is not bounded. This fact can be accounted for by  
18 assuming that the bare frequency is a function of the number of neighbors,  
19  $\hat{\alpha} = \hat{\alpha}(i)$ , such that  $\frac{d\hat{\alpha}}{di} < 0$  and becomes null for a finite value of  $i$ . Again, for  
20 the sake of simplicity, we assume that up to first order in  $i$ :  $\hat{\alpha} = \alpha(N_{max} - i)$ ,  
21 where  $N_{max}$  is the asymptotic, maximum, number of 3D neighbors a cell can  
22 possibly have. Summarizing, we assume that the apico-basal intercalation rate  
23  $r_{i,i+1}$  reads,

$$24 \quad r_{i,i+1} = \alpha(N_{max} - i)e^{-i\beta} \quad (18)$$

25 Under these conditions, the Kolmogorov equation reads,

$$26 \quad \frac{dP_m(s)}{ds} = \alpha(N_{max} - (m-1))e^{-\beta(m-1)}P_{m-1}(s) - \alpha(N_{max} - m)e^{-\beta m}P_m(s)$$

27 (19)

28 On the other hand, the equation satisfied by the average number of  
29 accumulated 3D neighbors,  $\langle n_{3D} \rangle = \langle m \rangle$ , reads,

$$1 \quad \frac{d\langle m(s) \rangle}{ds} = \sum_m m \frac{dP_m(s)}{ds} = \sum_m r_{m,m+1} P_m(s) = \langle r_{m,m+1} \rangle \quad (20)$$

2 Alternatively, in order to obtain an analytical expression able to recapitulate,  
 3 effectively, the mathematical principle that govern the net gain of 3D  
 4 neighbors, we perform the following approximations. First, we perform a  
 5 mean-field-like approximation, i.e.,  $\langle F(m) \rangle \approx F(\langle m \rangle)$ ,

$$6 \quad \frac{d\langle m \rangle}{ds} \approx \alpha (\langle N_{max} \rangle - \langle m \rangle) e^{-\beta \langle m \rangle} \quad (21)$$

7 Where  $\langle N_{max} \rangle$  is the limiting average cellular connectivity. Second, since  $\beta <$   
 8  $1$ ,

$$9 \quad \frac{d\langle m \rangle}{ds} \approx \alpha (\langle N_{max} \rangle - \langle m \rangle) (1 - \beta \langle m \rangle) + \mathcal{O}(\beta^2) \quad (22)$$

10 Equation (21) is formally a logistic-like growth equation,

$$11 \quad \frac{d\langle m \rangle}{ds} = \frac{b}{c(b-d)} (\langle N_{max} \rangle - \langle m \rangle) \left( 1 - \frac{d}{bN_{max}} \langle m \rangle \right) \quad (23)$$

12 that has as solution,

$$13 \quad \langle m(s) \rangle = \langle N_{max} \rangle \frac{1 + b e^{-\frac{s}{c}}}{1 + d e^{-\frac{s}{c}}} \quad (24)$$

14 Thus, if  $c > 0$  then  $\lim_{s \rightarrow \infty} \langle m(s) \rangle = \langle N_{max} \rangle$ . The parameters  $b$ ,  $c$ , and  $d$  are  
 15 further constrained by the following facts:  $\frac{d\langle m \rangle}{ds} > 0$  (3D neighbors can only  
 16 accumulate) and  $\frac{d^2\langle m \rangle}{ds^2} < 0$  (“poor get richer” principle). Moreover, if we impose  
 17 the condition  $\langle m(1) \rangle = 6$  (the average number of neighbors in the apical  
 18 surface is 6) these parameters are not independent since,

$$19 \quad b = \frac{6d - (\langle N_{max} \rangle - 6)e^{\frac{1}{c}}}{\langle N_{max} \rangle} \quad (25)$$

20 All the above implies that the logistic-like fitting function, Eq. (24), describes,  
 21 approximately but effectively, the analytical mathematical law (“Flintstone’s  
 22 law”) underlying the 3D average connectivity if the following conditions hold,  
 23 either  $-1 < d < 0$  or  $c \ln(-d) < 1$  if  $d < -1$ .

24 The relation between the fitting parameters of the logistic fitting with  $\alpha$  and  $\beta$   
 25 are,



1 
$$\alpha = \frac{b}{c(b-d)} \quad (26)$$

2 
$$\beta = \frac{d}{b\langle N_{max} \rangle} \quad (27)$$

3 For finding the parameters  $\alpha$  and  $\beta$  in *in silico* tubes and salivary glands we  
4 then implemented two possible approaches. On the one hand, we  
5 implemented an error minimization algorithm that recursively solved,  
6 numerically, Eq. (20) to obtain  $\langle m(s) \rangle = \sum_m m P_m(s)$  taking also into account  
7 the normalization condition  $\sum_{m=1}^{\infty} P_m(s) = 1$  (code available at  
8 <https://osf.io/nd5t6>).

9 On the other hand, we obtained values using the fitting logistic function Eq.  
10 (24). We notice that the values obtained through the first method are exact as  
11 compared to the values obtained from the fitting that are based on a series of  
12 approximations as explained above (see **Table S1**).

13 The values of  $\alpha$  and  $\beta$  are obtained from the exact methodology were further  
14 used to compare the predicted probability distribution of having  $m$   
15 accumulated neighbors for a given value of  $s$ :  $P_m(s)$ . We evaluated the relative  
16 error of this prediction with respect to the actual distribution from data,  
17  $P_m^{actual}(s)$ , by computing  $\varepsilon^2 = \frac{1}{2} \sum_m \left( P_m^{actual}(s) - P_m(s) \right)^2$ . This quantity is  
18 normalized such that in case of the following situation of full disagreement  
19 between the distributions,  $P_m^{actual}(s) = \delta_{m,i}$  and  $P_m(s) = \delta_{m,j}$  with  $i \neq j$ ,  
20 provides  $\varepsilon^2 = 1$  (i.e., 100% error).

21

## 22 **Quantitative characterization of spreading in neighbor exchange** 23 **distributions between apical and basal surfaces**

24 In order to characterize the spreading away from the diagonal in neighbor  
25 exchange distributions between apical and basal surfaces, **Fig. 2a-b**, we  
26 followed the same approach used to quantify intrinsic noise during gene  
27 expression processes (see (Elowitz, 2002)). Thus,  $\eta^2 = \frac{\langle (n_a - n_b)^2 \rangle}{2\langle n_a \rangle \langle n_b \rangle}$  where  
28  $\langle z(n_a, n_b) \rangle = \sum_{n_a, n_b} z(n_a, n_b) p(n_a, n_b)$ ;  $z$  representing any function of  $n_a$  and  $n_b$   
29 and  $p(n_a, n_b)$  being the probability of neighbor exchange events.

## 30 **Logistic data fitting**

1 To obtain the logistic function that fit best our data points, we analyzed all the  
2 possible parameters combination and achieved the global minimum solution.  
3 This 'fit' was based on the 'least squares' method and minimizes the residual  
4  $r = \sum_{i=1}^n (y_i - y_i')^2$  where,  $y_i$  and  $y_i'$  stand for the observed values and the  
5 fitted ones, respectively. The logistic equation (Eq. (24)):

$$6 \quad f(s) = \langle N_{max} \rangle \frac{1 + b e^{-\frac{s}{c}}}{1 + d e^{-\frac{s}{c}}} \quad (28)$$

7 was then fitted to find the average 3D cell connectivity, but with a series of  
8 constraints on the parameters (as explained above):  $\langle f(s=1) \rangle = 6$ ,  $c >$   
9  $0$ ,  $d < 0$ ,  $\langle N_{max} \rangle \geq 0$ ,  $d > b$  and if  $d < -1$  then  $c \ln(-d) < 1$ . The goodness  
10 of fitting was estimated by means of the coefficient of determination,  $R^2$ .

11

## 12 **Data availability**

13 All the necessary material to reproduce this study is available at the Center for  
14 Open Science repository: <https://osf.io/nd5t6>.

15

16

## 1 REFERENCES

- 2 Aldaz S, Escudero LM & Freeman M (2013) Dual role of myosin II during  
3 *Drosophila* imaginal disc metamorphosis. *Nat. Commun.* **4**: 1761
- 4 Alt S, Ganguly P & Salbreux G (2017) Vertex models: from cell mechanics to  
5 tissue morphogenesis. *Philos. Trans. R. Soc. B Biol. Sci.* **372**: 20150520
- 6 Ambrosini A, Gracia M, Proag A, Rayer M, Monier B & Suzanne M (2017)  
7 Apoptotic forces in tissue morphogenesis. *Mech. Dev.* **144**: 33–42
- 8 Arganda-Carreras I, Kaynig V, Rueden C, Eliceiri KW, Schindelin J, Cardona  
9 A & Sebastian Seung H (2017) Trainable Weka Segmentation: a machine  
10 learning tool for microscopy pixel classification. *Bioinformatics* **33**: 2424–  
11 2426
- 12 Bassel GW, Stamm P, Mosca G, Barbier de Reuille P, Gibbs DJ, Winter R,  
13 Janka A, Holdsworth MJ & Smith RS (2014) Mechanical constraints  
14 imposed by 3D cellular geometry and arrangement modulate growth  
15 patterns in the *Arabidopsis* embryo. *Proc. Natl. Acad. Sci.* **111**: 8685–  
16 8690
- 17 Bertet C, Sulak L & Lecuit T (2004) Myosin-dependent junction remodelling  
18 controls planar cell intercalation and axis elongation. *Nature* **429**: 667–  
19 671
- 20 Bi D, Lopez JH, Schwarz JM & Lisa Manning M (2014) Energy barriers and  
21 cell migration in densely packed tissues. *Soft Matter* **10**: 1885–1890
- 22 Bi D, Lopez JH, Schwarz JM & Manning ML (2015) A density-independent  
23 rigidity transition in biological tissues. *Nat. Phys.* **11**: 1074–1079
- 24 Bonnefont X, Lacampagne A, Sanchez-Hormigo A, Fino E, Creff A, Mathieu  
25 M-N, Smallwood S, Carmignac D, Fontanaud P, Travo P, Alonso G,  
26 Courtois-Coutry N, Pincus SM, Robinson ICAF & Mollard P (2005)  
27 Revealing the large-scale network organization of growth hormone-  
28 secreting cells. *Proc. Natl. Acad. Sci.* **102**: 16880–16885
- 29 Campàs O, Mammoto T, Hasso S, Sperling RA, O'Connell D, Bischof AG,  
30 Maas R, Weitz DA, Mahadevan L & Ingber DE (2014) Quantifying cell-  
31 generated mechanical forces within living embryonic tissues. *Nat.*  
32 *Methods* **11**: 183–189
- 33 Canela-Xandri O, Sagués F, Casademunt J & Buceta J (2011) Dynamics and  
34 Mechanical Stability of the Developing Dorsoventral Organizer of the  
35 Wing Imaginal Disc. *PLoS Comput. Biol.* **7**: e1002153
- 36 Clevers H (2016) Modeling Development and Disease with Organoids. *Cell*  
37 **165**: 1586–1597
- 38 Colas J-F & Schoenwolf GC (2001) Towards a cellular and molecular  
39 understanding of neurulation. *Dev. Dyn.* **221**: 117–145
- 40 Curran S, Strandkvist C, Bathmann J, de Gennes M, Kabla A, Salbreux G &  
41 Baum B (2017) Myosin II Controls Junction Fluctuations to Guide  
42 Epithelial Tissue Ordering. *Dev. Cell* **43**: 480-492.e6
- 43 Elowitz MB (2002) Stochastic Gene Expression in a Single Cell. *Science* (80-  
44 ). **297**: 1183–1186
- 45 Farhadifar R, Röper J-C, Aigouy B, Eaton S & Jülicher F (2007) The Influence  
46 of Cell Mechanics, Cell-Cell Interactions, and Proliferation on Epithelial

- 1       Packing. *Curr. Biol.* **17**: 2095–2104
- 2       Fletcher AG, Osterfield M, Baker RE & Shvartsman SY (2014) Vertex models  
3       of epithelial morphogenesis. *Biophys. J.* **106**: 2291–2304
- 4       Gibson MC, Patel AB, Nagpal R & Perrimon N (2006) The emergence of  
5       geometric order in proliferating metazoan epithelia. *Nature* **442**: 1038–  
6       1041
- 7       Gibson WT, Veldhuis JH, Rubinstein B, Cartwright HN, Perrimon N, Brodland  
8       GW, Nagpal R & Gibson MC (2011) Control of the mitotic cleavage plane  
9       by local epithelial topology. *Cell* **144**: 427–438
- 10      Gilbert SF & Barresi MJF (2016) *Developmental biology* 11th ed. Sunderland,  
11      MA Sinauer Associates
- 12      Girdler GC & Röper K (2014) Controlling cell shape changes during salivary  
13      gland tube formation in *Drosophila*. *Semin. Cell Dev. Biol.* **31**: 74–81
- 14      Gómez-Gálvez P, Vicente-Munuera P, Tagua A, Forja C, Castro AMAM,  
15      Letrán M, Valencia-Expósito A, Grima C, Bermúdez-Gallardo M, Serrano-  
16      Pérez-Higueras Ó, Cavodeassi F, Sotillos S, Martín-Bermudo MDMD,  
17      Márquez A, Buceta J & Escudero LM (2018) Scutoids are a geometrical  
18      solution to three-dimensional packing of epithelia. *Nat. Commun.* **9**: 2960
- 19      Heller D, Hoppe A, Restrepo S, Gatti L, Tournier AL, Tapon N, Basler K & Mao  
20      Y (2016) EpiTools: An Open-Source Image Analysis Toolkit for  
21      Quantifying Epithelial Growth Dynamics. *Dev Cell* **36**: 103–116
- 22      Hirashima T & Adachi T (2019) Polarized cellular mechano-response system  
23      for maintaining radial size in developing epithelial tubes. *Development*  
24      **146**: dev181206
- 25      Honda H (1978) Description of cellular patterns by Dirichlet domains: the two-  
26      dimensional case. *J Theor Biol* **72**: 523–543
- 27      Huch M, Knoblich JA, Lutolf MP & Martinez-Arias A (2017) The hope and the  
28      hype of organoid research. *Dev.* **144**: 938–941
- 29      Huebner RJ & Ewald AJ (2014) Cellular foundations of mammary  
30      tubulogenesis. *Semin. Cell Dev. Biol.* **31**: 124–131
- 31      Inoue Y, Tateo I & Adachi T (2019) Epithelial tissue folding pattern in confined  
32      geometry. *Biomech. Model. Mechanobiol.*
- 33      Iruela-Arispe ML & Beitel GJ (2013) Tubulogenesis. *Development* **140**: 2851–  
34      2855
- 35      Irvine KD & Wieschaus E (1994) Cell intercalation during *Drosophila*  
36      germband extension and its regulation by pair-rule segmentation genes.  
37      *Development* **120**: 827–841
- 38      Khan Z, Wang Y-C, Wieschaus EF & Kaschube M (2014) Quantitative 4D  
39      analyses of epithelial folding during *Drosophila* gastrulation. *Development*  
40      **141**: 2895–2900
- 41      Latorre E, Kale S, Casares L, Gómez-González M, Uroz M, Valon L, Nair R V.,  
42      Garreta E, Montserrat N, del Campo A, Ladoux B, Arroyo M & Trepast X  
43      (2018) Active superelasticity in three-dimensional epithelia of controlled  
44      shape. *Nature* **563**: 203–208
- 45      Leptin M & Grunewald B (1990) Cell shape changes during gastrulation in  
46      *Drosophila*. *Development* **110**: 73–84

- 1 Lewis FT (1928) The correlation between cell division and the shapes and  
2 sizes of prismatic cells in the epidermis of cucumis. *Anatom. Rec.* **38**:  
3 341–376
- 4 Lloyd S (1982) Least squares quantization in PCM. *IEEE Trans. Inf. Theory*  
5 **28**: 129–137
- 6 Machado S, Mercier V & Chiaruttini N (2019) LimeSeg: a coarse-grained lipid  
7 membrane simulation for 3D image segmentation. *BMC Bioinformatics*  
8 **20**: 2
- 9 Mao Y, Tournier AL, Hoppe A, Kester L, Thompson BJ & Tapon N (2013)  
10 Differential proliferation rates generate patterns of mechanical tension that  
11 orient tissue growth. *EMBO J.* **32**: 2790–2803
- 12 Messal HA, Alt S, Ferreira RMM, Gribben C, Wang VM-Y, Cotoi CG, Salbreux  
13 G & Behrens A (2019) Tissue curvature and apicobasal mechanical  
14 tension imbalance instruct cancer morphogenesis. *Nature* **566**: 126
- 15 Misra M, Audoly B & Shvartsman SY (2017) Complex structures from  
16 patterned cell sheets. *Philos. Trans. R. Soc. B Biol. Sci.* **372**: 20150515
- 17 Mongera A, Rowghanian P, Gustafson HJ, Shelton E, Kealhofer DA, Carn EK,  
18 Serwane F, Lucio AA, Giammona J & Campàs O (2018) A fluid-to-solid  
19 jamming transition underlies vertebrate body axis elongation. *Nature* **561**:  
20 401–405
- 21 Mughal A, Cox SJ, Weaire D, Burke SR & Hutzler S (2018) Demonstration and  
22 interpretation of ‘scutoid’ cells formed in a quasi-2D soap froth. *Philos.*  
23 *Mag. Lett.* **98**: 358–364
- 24 Nelson CM (2009) Geometric control of tissue morphogenesis. *Biochim.*  
25 *Biophys. Acta - Mol. Cell Res.* **1793**: 903–910
- 26 Nelson CM, Jean RP, Tan JL, Liu WF, Sniadecki NJ, Spector AA & Chen CS  
27 (2005) Emergent patterns of growth controlled by multicellular form and  
28 mechanics. *Proc. Natl. Acad. Sci.* **102**: 11594–11599
- 29 Okuda S, Kuranaga E & Sato K (2019) Apical Junctional Fluctuations Lead to  
30 Cell Flow while Maintaining Epithelial Integrity. *Biophys. J.* **116**: 1159–  
31 1170
- 32 Pérez-González C, Alert R, Blanch-Mercader C, Gómez-González M,  
33 Kolodziej T, Bazellieres E, Casademunt J & Trepát X (2019) Active  
34 wetting of epithelial tissues. *Nat. Phys.* **15**: 79–88
- 35 Pilot F & Lecuit T (2005) Compartmentalized morphogenesis in epithelia: from  
36 cell to tissue shape. *Dev Dyn* **232**: 685–694
- 37 Reinhardt K (1918) Über die Zerlegung der Ebene in Polygone.
- 38 Röper K (2018) Quantitative Imaging and the Effect of Tissue Topology on  
39 Morphogenesis. *Dev. Cell* **47**: 537–538
- 40 Rupprecht JF, Ong KH, Yin J, Huang A, Dinh HHQ, Singh AP, Zhang S, Yu W  
41 & Saunders TE (2017) Geometric constraints alter cell arrangements  
42 within curved epithelial tissues. *Mol. Biol. Cell* **28**: 3582–3594
- 43 Sanchez-Corrales YE, Blanchard GB & Röper K (2018) Radially patterned cell  
44 behaviours during tube budding from an epithelium. *Elife* **7**: e35717
- 45 Sánchez-Gutiérrez D, Tozluoglu M, Barry JD, Pascual A, Mao Y & Escudero  
46 LM (2016) Fundamental physical cellular constraints drive self-  
47 organization of tissues. *EMBO J.* **35**: 77–88

- 1 Schindelin J, Arganda-Carreras I, Frise E, Kaynig V, Longair M, Pietzsch T,  
2 Preibisch S, Rueden C, Saalfeld S, Schmid B, Tinevez J-Y, White DJ,  
3 Hartenstein V, Eliceiri K, Tomancak P & Cardona A (2012) Fiji: an open-  
4 source platform for biological-image analysis. *Nat. Methods* **9**: 676–682
- 5 Schutgens F, Rookmaaker MB, Margaritis T, Rios A, Ammerlaan C, Jansen J,  
6 Gijzen L, Vormann M, Vonk A, Viveen M, Yengej FY, Derakhshan S, de  
7 Winter-de Groot KM, Artegiani B, van Boxtel R, Cuppen E, Hendrickx  
8 APA, van den Heuvel-Eibrink MM, Heitzer E, Lanz H, et al (2019)  
9 Tubuloids derived from human adult kidney and urine for personalized  
10 disease modeling. *Nat. Biotechnol.* **37**: 303–313
- 11 Shahbazi MN, Siggia ED & Zernicka-Goetz M (2019) Self-organization of stem  
12 cells into embryos: A window on early mammalian development. *Science*  
13 (80-. ). **364**: 948–951
- 14 Sharma P, Saraswathy VM, Xiang L & Furthauer M (2019) Delta/Notch  
15 signaling controls neuroepithelial morphogenesis in the zebrafish spinal  
16 cord. *bioRxiv*: 517714
- 17 Siedlik MJ, Manivannan S, Kevrekidis IG & Nelson CM (2017) Cell Division  
18 Induces and Switches Coherent Angular Motion within Bounded Cellular  
19 Collectives. *Biophys. J.* **112**: 2419–2427
- 20 Spencer MA, Jabeen Z & Lubensky DK (2017) Vertex stability and topological  
21 transitions in vertex models of foams and epithelia. *Eur. Phys. J. E* **40**: 2
- 22 Sugimura K, Lenne PF & Graner F (2016) Measuring forces and stresses in  
23 situ in living tissues. *Development* **143**: 186–196
- 24 Swanson LE & Beitel GJ (2006) Tubulogenesis: an inside job. *Curr Biol* **16**:  
25 R51-3
- 26 Tetley RJ, Staddon MF, Heller D, Hoppe A, Banerjee S & Mao Y (2019)  
27 Tissue fluidity promotes epithelial wound healing. *Nat. Phys.* **15**: 1195–  
28 1203
- 29 Thompson DWD (1945) On growth and form Cambridge university press
- 30 Trepat X, Wasserman MR, Angelini TE, Millet E, Weitz DA, Butler JP &  
31 Fredberg JJ (2009) Physical forces during collective cell migration. *Nat.*  
32 *Phys.* **5**: 426–430
- 33 Tung JJ, Tattersall IW & Kitajewski J (2012) Tips, Stalks, Tubes: Notch-  
34 Mediated Cell Fate Determination and Mechanisms of Tubulogenesis  
35 during Angiogenesis. *Cold Spring Harb. Perspect. Med.* **2**: a006601–  
36 a006601
- 37 Wetzel G (1926) Zur entwicklungsmechanischen Analyse des einfachen  
38 prismatischen Epithels. *Wilhelm Roux Arch. für Entwicklungsmechanik*  
39 *der Org.* **107**: 177–185
- 40 Yang R, Li E, Kwon Y-J, Mani M & Beitel GJ (2019) QuBiT: a quantitative tool  
41 for analyzing epithelial tubes reveals unexpected patterns of organization  
42 in the Drosophila trachea. *Development* **146**: dev172759
- 43 Yang X, Bi D, Czajkowski M, Merkel M, Manning ML & Marchetti MC (2017)  
44 Correlating cell shape and cellular stress in motile confluent tissues. *Proc.*  
45 *Natl. Acad. Sci.* **114**: 12663–12668
- 46  
47



1 **Figure 1. Analysis of apico-basal cell intercalations in the Voronoi**  
2 **tubular model**

3 **a)** Scutoids (left) entail apico-basal intercalations among packing cells that can  
4 be envisioned as *spatial* T1 transitions to exchange neighbors (right). The  
5 green and the red cells are neighbors in basal (but not in apical) while the  
6 opposite is true for the blue and the yellow cells. **b)** Voronoi *in silico* tubes with  
7 different surface ratios,  $s_b$ :  $s_b = 2$  indigo blue;  $s_b = 5$ , dark blue (apical  
8 surface, light blue). **c)** For a given radial section (plane), cell boundaries  
9 emerge by applying a Voronoi tessellation to a number of seeds located in the  
10 plane. In the V1 (Voronoi 1) model seeds are randomly distributed. By  
11 applying iteratively the Lloyd algorithm (left to right) the topological disorder  
12 diminishes (**Materials and Methods**). **d)** The density plot shows the average  
13 number of apico-basal intercalations per cell in *in silico* tubes ( $n = 20$ ) as a  
14 function of the surface ratio and the Voronoi class.

15



1 **Figure 2. Three-dimensional packing and connectivity properties of the**  
2 **Voronoi tubular model**

3 **a)** A schematic representation of a 3D histogram (density plot) where all cells  
4 have prismatic-like shapes (i.e., in the absence of scutoids). The histogram  
5 accounts for the probability that cells have  $n_a$  (number) of neighbors in the  
6 apical surface and  $n_b$  neighbors in the basal surface. If there are no scutoids,  
7 there are only contributions in the diagonal bins whereas if there are scutoids  
8 the distribution spreads away from the diagonal. **b)** 3D histograms of V5 tubes  
9 for increasing values of the surface ratio. The larger value of the spreading  
10 coefficient,  $\eta^2$ , (**Material and Methods**) indicates an increasing number of  
11 scutoids. **c)** and **d)** Density plots showing  $\eta^2$  (**c**) and the average number of  
12 3D neighbors,  $\langle n_{3D} \rangle$ , (**d**) as a function of the surface ratio and the Voronoi  
13 class in *in silico* tubes ( $n = 20$ ).  
14

1 **Figure 3. Cells in the Voronoi tubular model follow a “poor get richer”**  
2 **principle**

3 **a)** Average net gain of neighbors (density plot) with respect to the apical  
4 surface in Voronoi tubes with a surface ratio  $s_b = 5$  as a function of the  
5 Voronoi class and the apical polygonal class ( $n = 20$ ). Cells with a smaller  
6 polygonal class are more prone to gain neighbors. **b)** “Poor get richer”  
7 principle in V5 tubes with a surface ratio  $s_b = 5$ . The size of the circle accounts  
8 for the relative data count within each apical polygon class (numbers indicate  
9 the number of cells that gained 3D neighbors). The boxes indicate the  
10 25% – 75% percentile interval, black lines the mean values, gray lines the  
11 standard deviation, and the red dotted lines the statistical median.

1 **Box. In tubular geometries the 3D cellular connectivity gain decreases as**  
2 **the surface ratio increases and it is bounded.** In this example, the Y axis  
3 represents the longitudinal axis of tubes, while the X axis accounts for the  
4 Cartesian projection of the transversal axis of radial sections. From left to right  
5 different radial sections are represented as  $s$  increases (as indicated by the  
6 color gradient arrow: from light to dark blue). In **a)** three Voronoi seeds that  
7 correspond to neighboring cells at the apical surface,  $s = 1$ , define the triangle  
8  $ABC$ . Panels **b)** and **c)** track changes in the neighboring relations  
9 (accumulated neighbors) of cell  $A$  for two increasing values of  $s$ : 2 and 4.5  
10 (panels **b)** and **c)** respectively). As shown in **a)**, should a new neighboring cell,  
11  $D$ , of cell  $A$  appear due to an apico-basal intercalation, then its position must  
12 lie inside the parabola defined by the points  $A$ ,  $B$  and  $C$ , but outside the circle  
13 that these points define (white region), (see *Lemma 1*, **Material and**  
14 **Methods**). Regions accessible to new neighbors are then coded by the green  
15 shading in **a)-c)**. As  $s$  increases, see **b)**, and the cells  $A$ ,  $B$ ,  $C$ , and  $D$  become  
16 neighbors, then the parabolas and circles defined by  $ABD$  and  $ACD$  restrict the  
17 locations of possible new neighbors. This idea is further reinforced in panel **c)**:  
18 winning neighbor  $E$  set additional limits to the accessible locations of new  
19 neighbors. Thus, the potentiality of a connectivity gain by cell  $A$  due to apico-  
20 basal intercalations diminishes as the surface ratio increases and eventually  
21 becomes null: the number of 3D neighbors of a cell is bounded (**Materials and**  
22 **Methods**).  
23

1 **Figure 4. A probabilistic model reproduces the 3D cell connectivity**  
2 **behavior of epithelial tubes.**

3 **a)** Top: in tubular geometries, cell intercalations along the apico-basal axis can  
4 be visualized as non-reversible spatial T1 transitions (once a neighbor is won  
5 it cannot be lost). Bottom: the “poor get richer” principle suggests an  
6 increasing energetic cost (i.e., a larger activation energy) for recruiting new 3D  
7 neighbors. In our model,  $\beta$  accounts for the energetic cost per 3D neighbor to  
8 recruit a new neighbor (**Materials and Methods**). **b)** The energy landscape  
9 shown in **a)** can be modeled by a stochastic dynamics (a Kolmogorov rate  
10 equation) where cells increase their 3D neighbors with a probability per unit of  
11 surface ratio,  $r_{n,m}$ , that depends on the activation energy and the maximum  
12 cell connectivity  $N_{max}$  (**Material and Methods**). **c)** Comparison between  
13 results obtained in the Kolmogorov model and simulations of V5 *in silico* tubes.  
14 The left/center density plots represent the connectivity distribution (i.e., the  
15 fraction of cells with a given number of 3D neighbors) as a function of the  
16 radial expansion obtained in the Voronoi simulation (left) and as predicted by  
17 the Kolmogorov model (center); the purple open circles (left/right) indicate the  
18 average number of 3D neighbors per cell  $\langle n_{3D} \rangle$ ; the solid red line and the  
19 dashed white line (center/right) shows  $\langle n_{3D} \rangle$  as obtained by the Kolmogorov  
20 model and the Flinstones’ law respectively. The density plot on the right shows  
21 the difference between the predicted and the actual connectivity distributions  
22 and the corresponding error,  $\varepsilon^2$  (magenta lines), see **Fig. S3** and **Material and**  
23 **Methods**.

24

1 **Figure 5. Packing and connectivity analysis of *Drosophila's* salivary**  
2 **gland and comparison with the V8 model**

3 **a)** Full projection of a salivary gland (cell contours stained by Cy3-labeled  
4 phalloidin, **Materials and Methods**). **b)** Computer representation of the  
5 segmented salivary gland shown in **a)** (**Material and Methods**). **c)** 3D  
6 rendering of a representative segmented salivary gland: apical surface, light  
7 green; basal surface, dark green. **d)** Density plots of the distribution of  
8 neighbor exchanges between apical and basal surfaces as a function of the  
9 number of neighbors in apical,  $n_a$ , and basal,  $n_b$ , surfaces (as in **Fig. 2b**):  
10 salivary glands (left) and V8 tubes (right) with surface ratio  $s_b = 1.75$ . **e)**  
11 Comparison between results obtained in salivary glands (top) and the  
12 simulations of the V8 model (bottom) in regards of the 3D cellular connectivity  
13 as a function of the surface ratio (see Fig. **4c**).

14

15

16

1 **Figure S1. Scutoidal prevalence and relation between  $\langle n_{3D} \rangle$  and  $\langle i \rangle$ .**

2 **a)** The density plot shows the percentage of scutoidal cells in the tissue  
3 (scutoidal prevalence) as a function of the surface ratio (from  $s = 1$  to  $s = 4$   
4 with steps of 0.25) and the Voronoi class (same samples that in Fig. 1d). We  
5 notice that from  $s = 4$  onward, the scutoidal prevalence in all Voronoi  
6 diagrams is 100%. **b)** Average number of 3D neighbors,  $\langle n_{3D} \rangle$ , as a function of  
7 the average number of apico-basal intercalations per cell,  $\langle i \rangle$ , in Voronoi tubes  
8 (from  $s = 1$  to  $s = 10$  with steps of 0.5, 20 samples) and in salivary glands  
9 (from  $s = 1$  to  $s = 3.5$  with steps of 0.5, 20 samples).

10

11 **Figure S2. Poor get richer principle in Voronoi tubes.**

12 Average net gain of neighbors (density plot) with respect to the apical surface  
13 in Voronoi tubes with surface ratios  $s_b = 1.5$  and  $s_b = 2$  (**a**), and with respect  
14 to the basal surface for  $s_b = 5$  (**b**) as a function of the Voronoi and the  
15 polygonal class ( $n = 20$ ).

16

17 **Figure S3. Comparison between results obtained in the Kolmogorov**  
18 **model and simulations of V1 and V10 *in silico* tubes.**

19 As in **Fig. 3b**, the left/center density plots represent the connectivity  
20 distribution (i.e., the fraction of cells with a given number of 3D neighbors) as a  
21 function of the radial expansion obtained in the Voronoi simulation (left) and as  
22 predicted by the Kolmogorov model (center); the purple open circles (left/right)  
23 indicate the average number of 3D neighbors per cell  $\langle n_{3D} \rangle$ ; the solid red line  
24 and the dashed white line (center/right) shows  $\langle n_{3D} \rangle$  as obtained by the  
25 Kolmogorov model and the Flinstones' law respectively. The density plot on  
26 the right shows the difference between the predicted and the actual  
27 connectivity distributions and the corresponding error,  $\varepsilon^2$  (magenta lines).

28

29 **Figure S4. Polygon distribution in apical and basal surfaces and “poor**  
30 **get richer” principle: salivary gland and V8 tubes.**

31 **a)** Polygon distribution of salivary glands and Voronoi 8 (V8) *in silico* tubes: the  
32 error bar accounts for the standard deviation ( $n = 20$ ). **b)** Average net gain of  
33 neighbors (density plot) with respect to the apical surface in salivary glands

1 (top) and V8 tubes with a surface ratio  $s_b = 1.75$  (middle) and  $s_b = 4$  (bottom)  
2 as a function of the apical polygonal class ( $n = 20$ ). **c)** Absolute net gain of 3D  
3 neighbors as a function of the polygonal class in the apical surface (green:  
4 salivary gland; blue: V8 tubes). The size of the circle accounts for the relative  
5 data count within the apical polygon class (integer numbers indicate the  
6 number of cells that gained 3D neighbors). The boxes indicate the 25% – 75%  
7 percentile interval, black lines the mean values, gray lines the standard  
8 deviation, and the red dotted lines the statistical median. Cells with a smaller  
9 polygonal class are more prone to gain neighbors.

10

### 11 **Figure S5. Euler characteristic in scutoids.**

12 A scutoid solid can be simplified as a collection of vertexes (circles) that can  
13 be connected by straight edges. In the figure the green circle accounts of an  
14 apico-basal intercalation point. Alternatively, we can represent the solid as a  
15 connected plane graph. In both cases the Euler characteristic is 2.

16

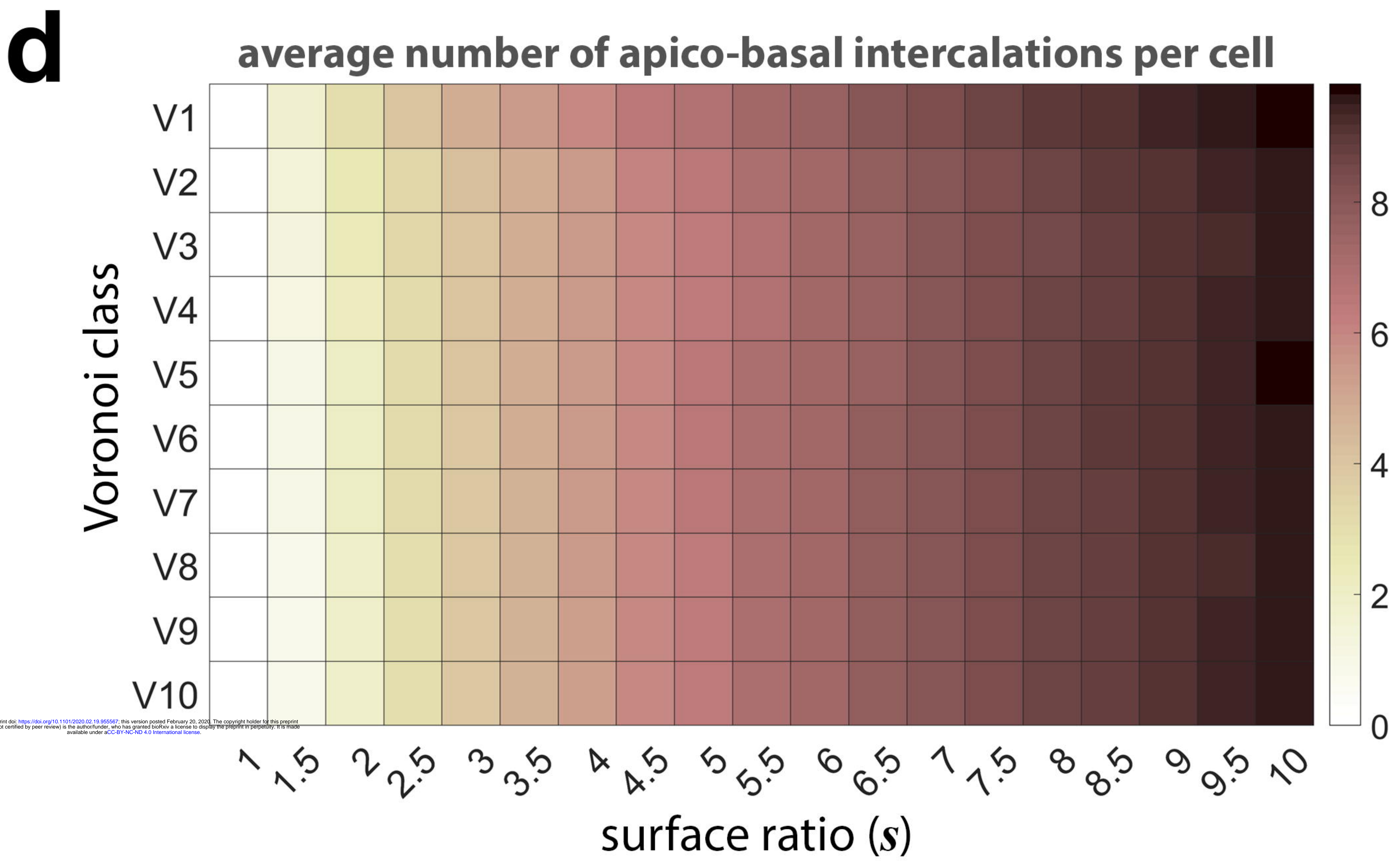
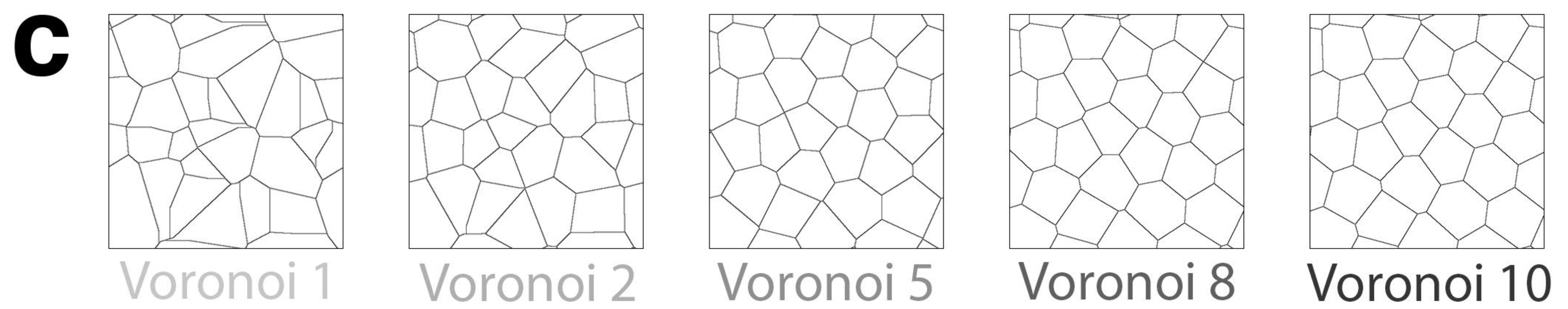
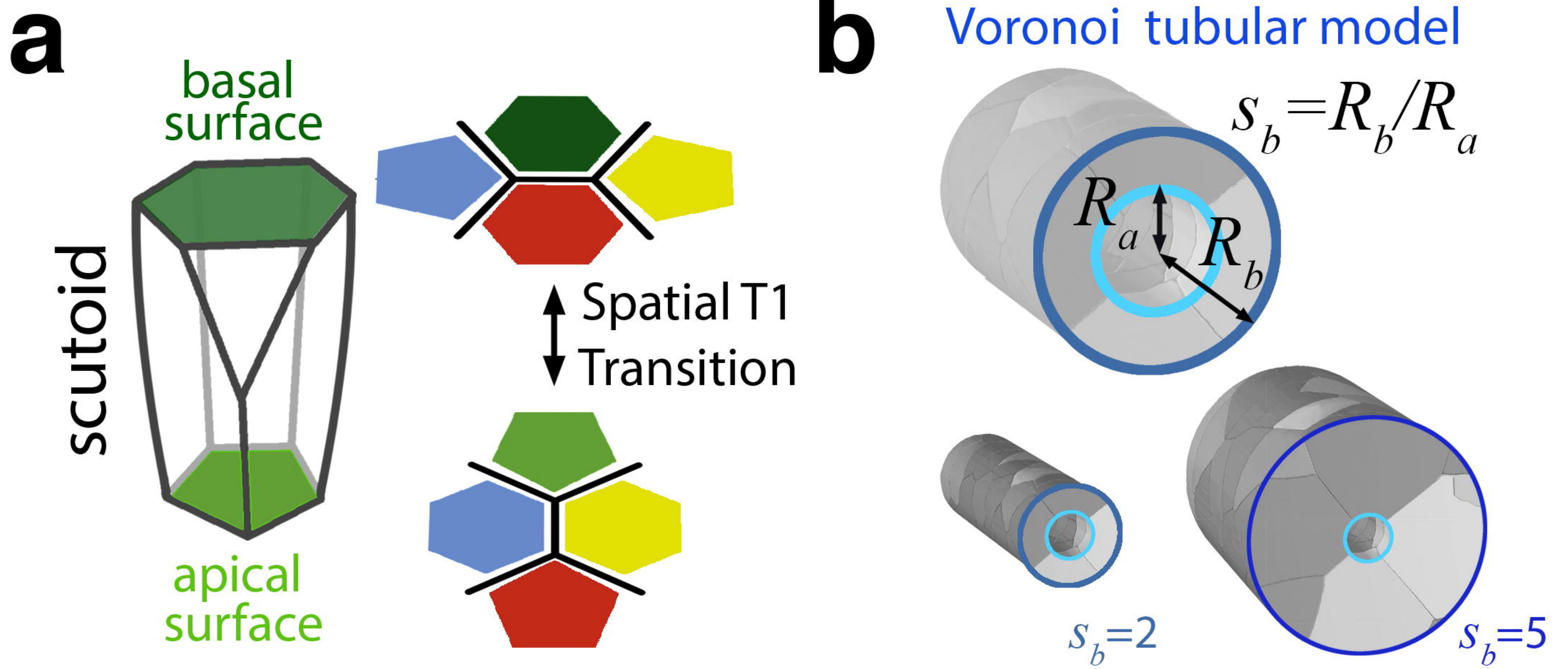
### 17 **Table S1. Fitting parameters (Flintstones' law and Kolmogorov model)** 18 **and spreading quantification in Voronoi tubes and salivary glands.**

19 Tab 1 (**Flintstones**) shows the independent fitting parameter values  
20 ( $c, d, \langle N_{max} \rangle$ ), the values of  $b, \langle n_{3D} \rangle$  for different, relevant, values of the surface  
21 ratio, and the estimated values of  $\alpha$  and  $\beta$  (**Materials and Methods**). Tab 2  
22 (**Kolmogorov**) shows the independent fitting parameter values ( $\alpha, \beta, \langle N_{max} \rangle$ ).  
23 Tab 3 (**Spreading**) shows the spreading values of the 3D histograms of  
24 neighbor exchange between basal and apical surfaces (**Materials and**  
25 **Methods**).

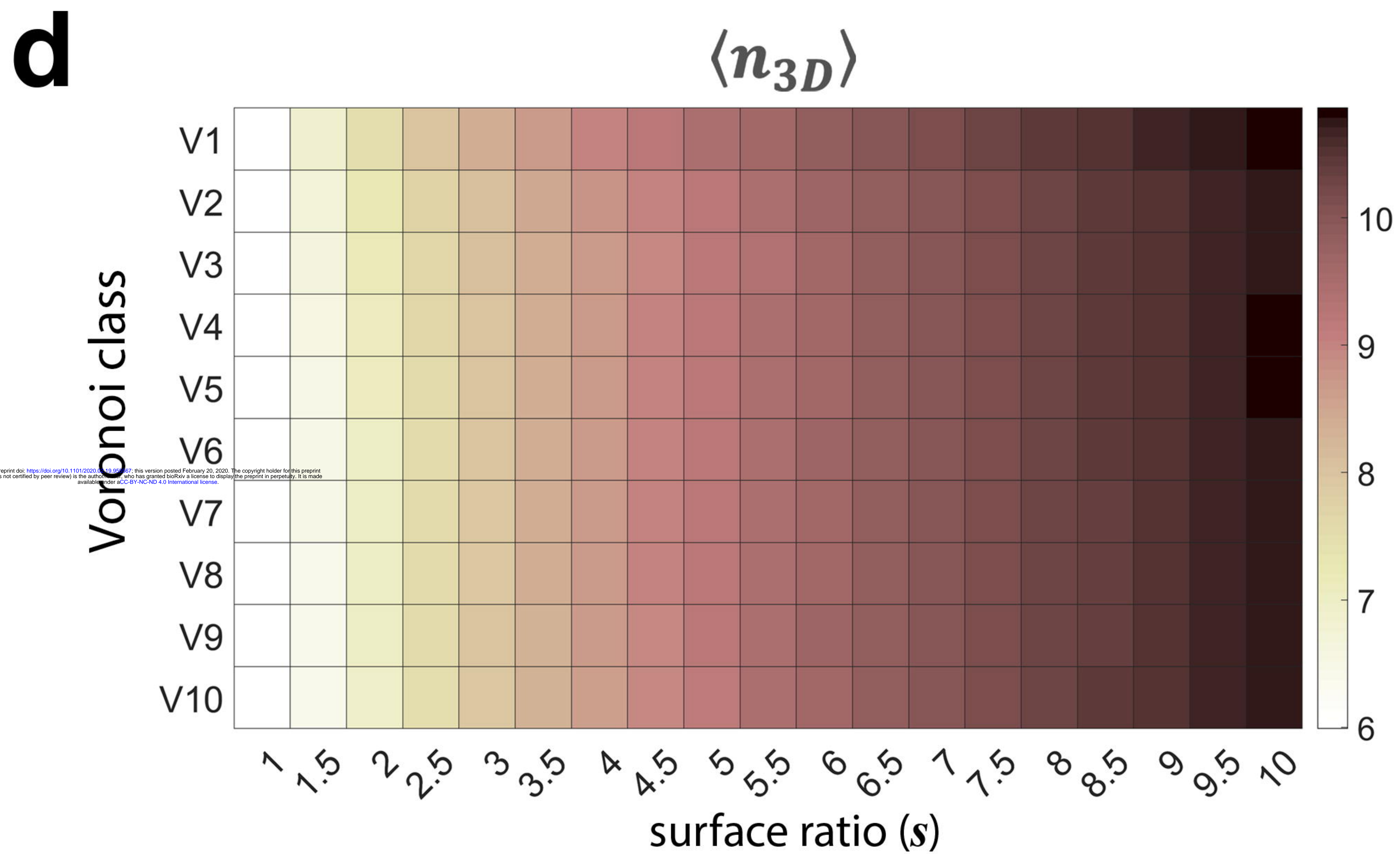
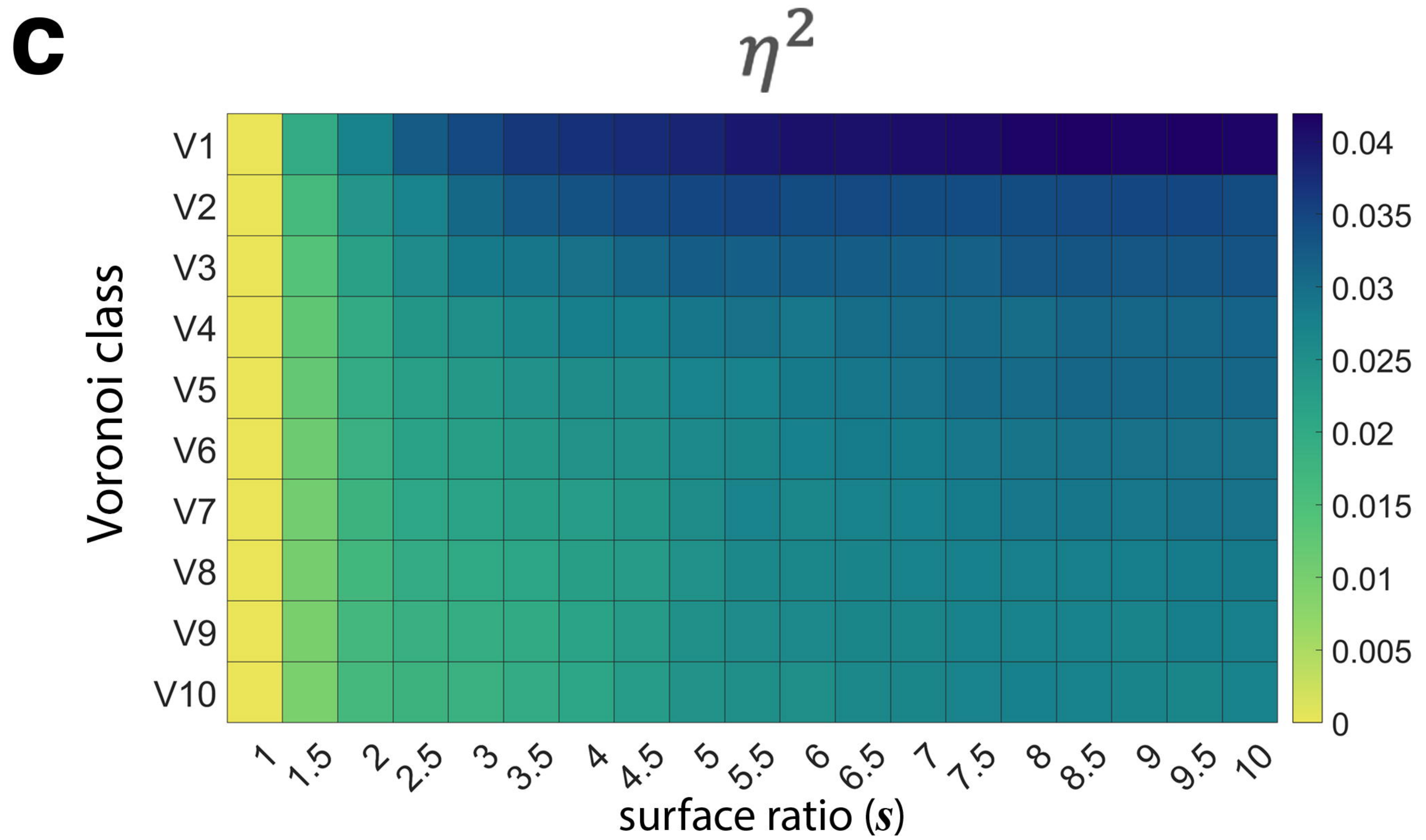
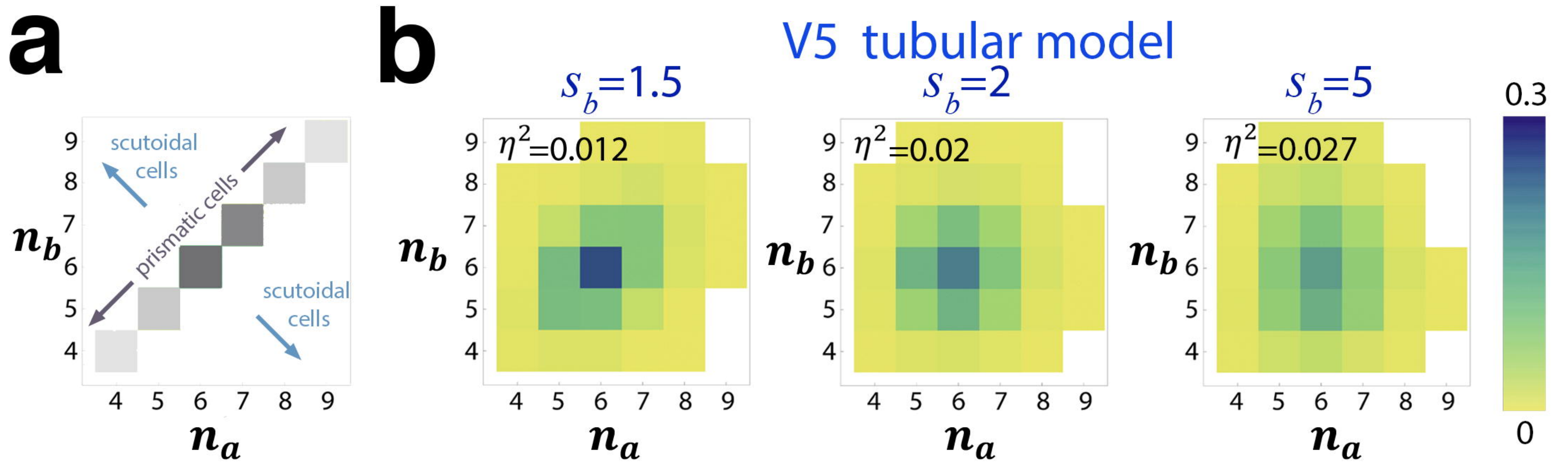
26

27

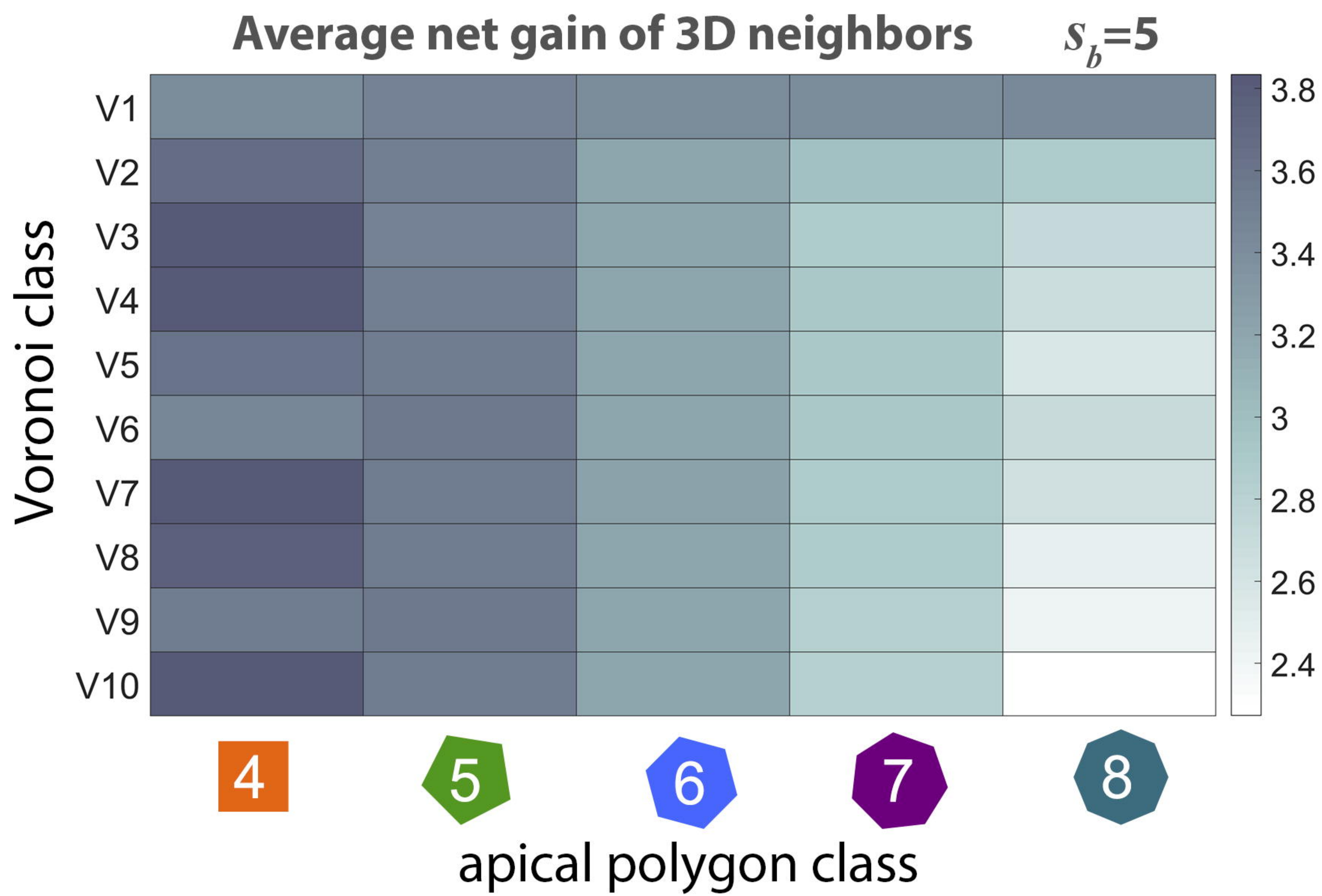
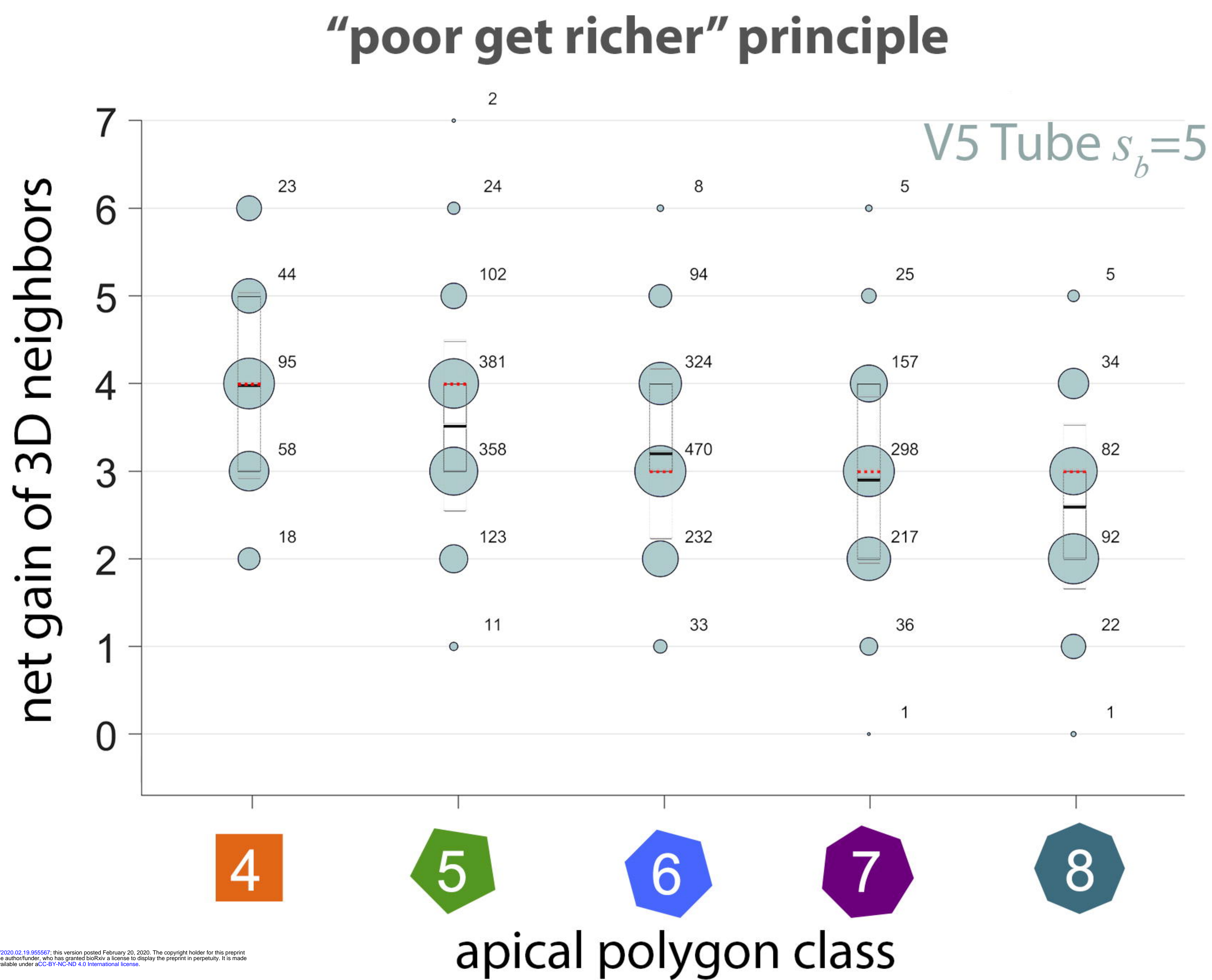




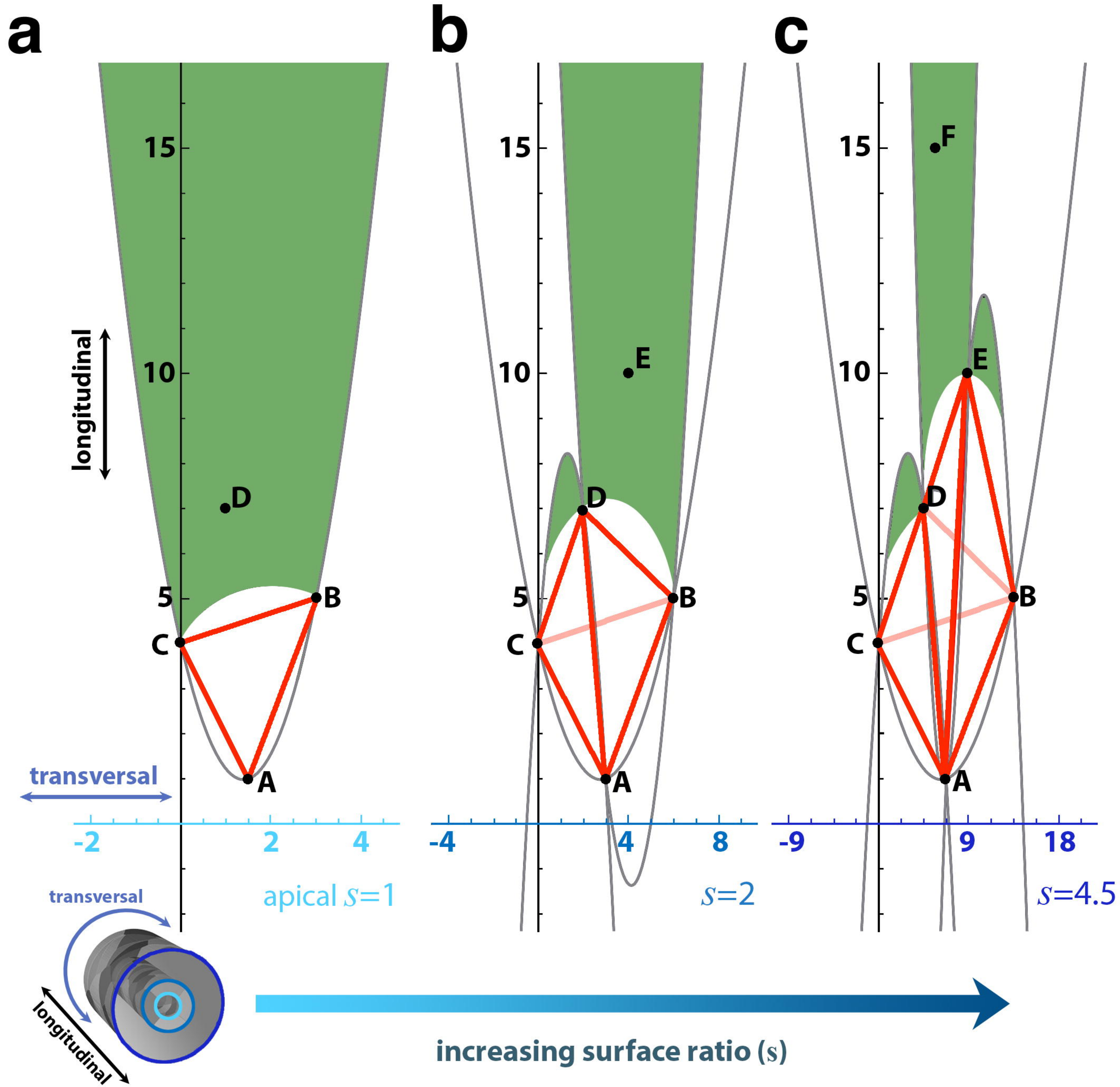




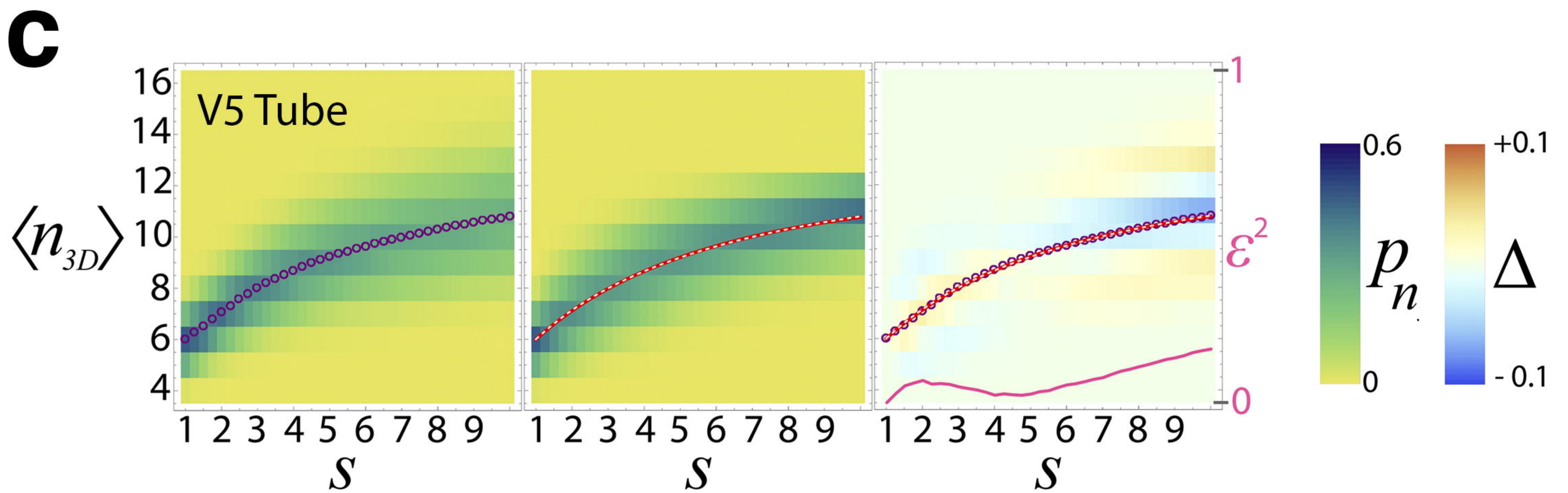
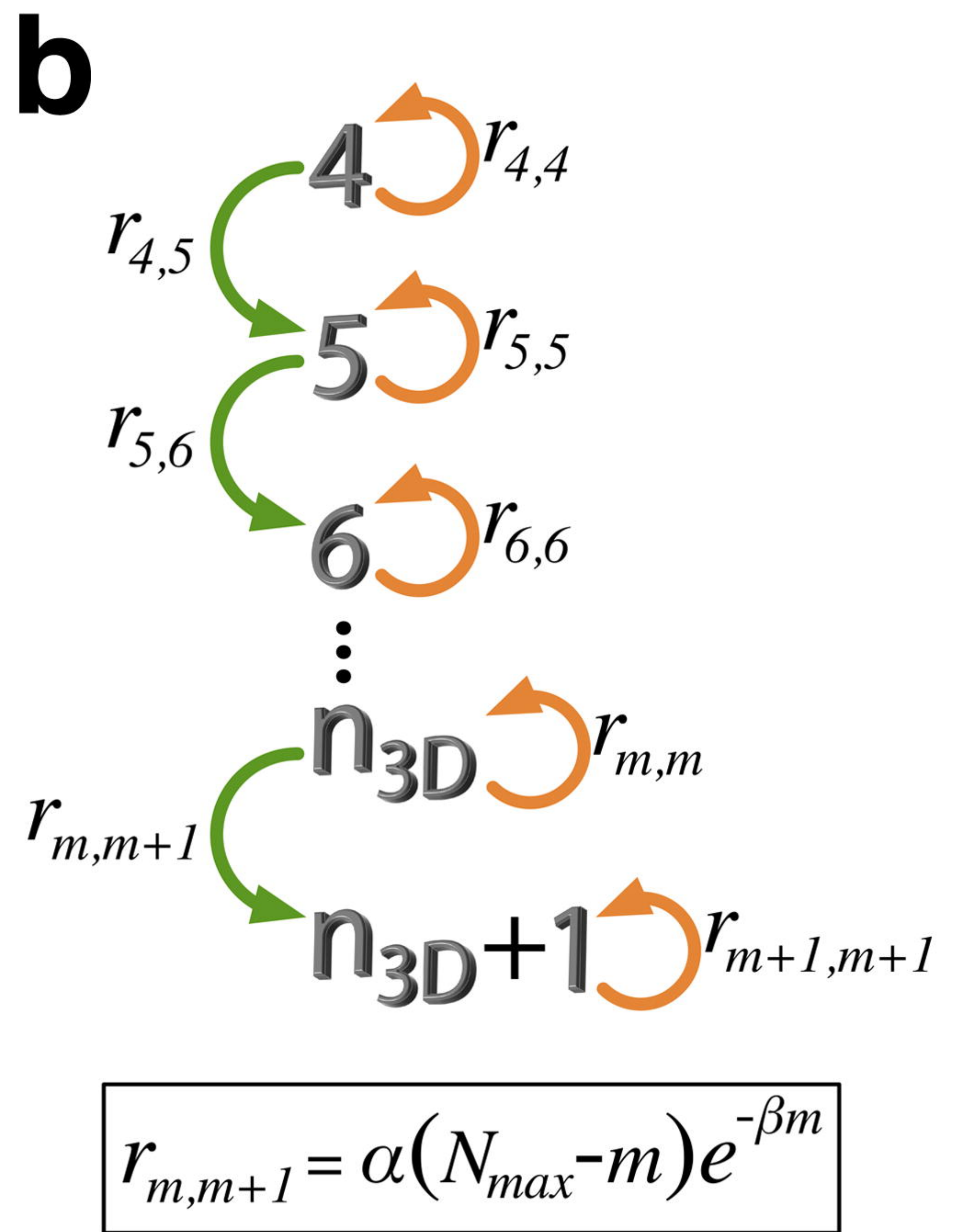
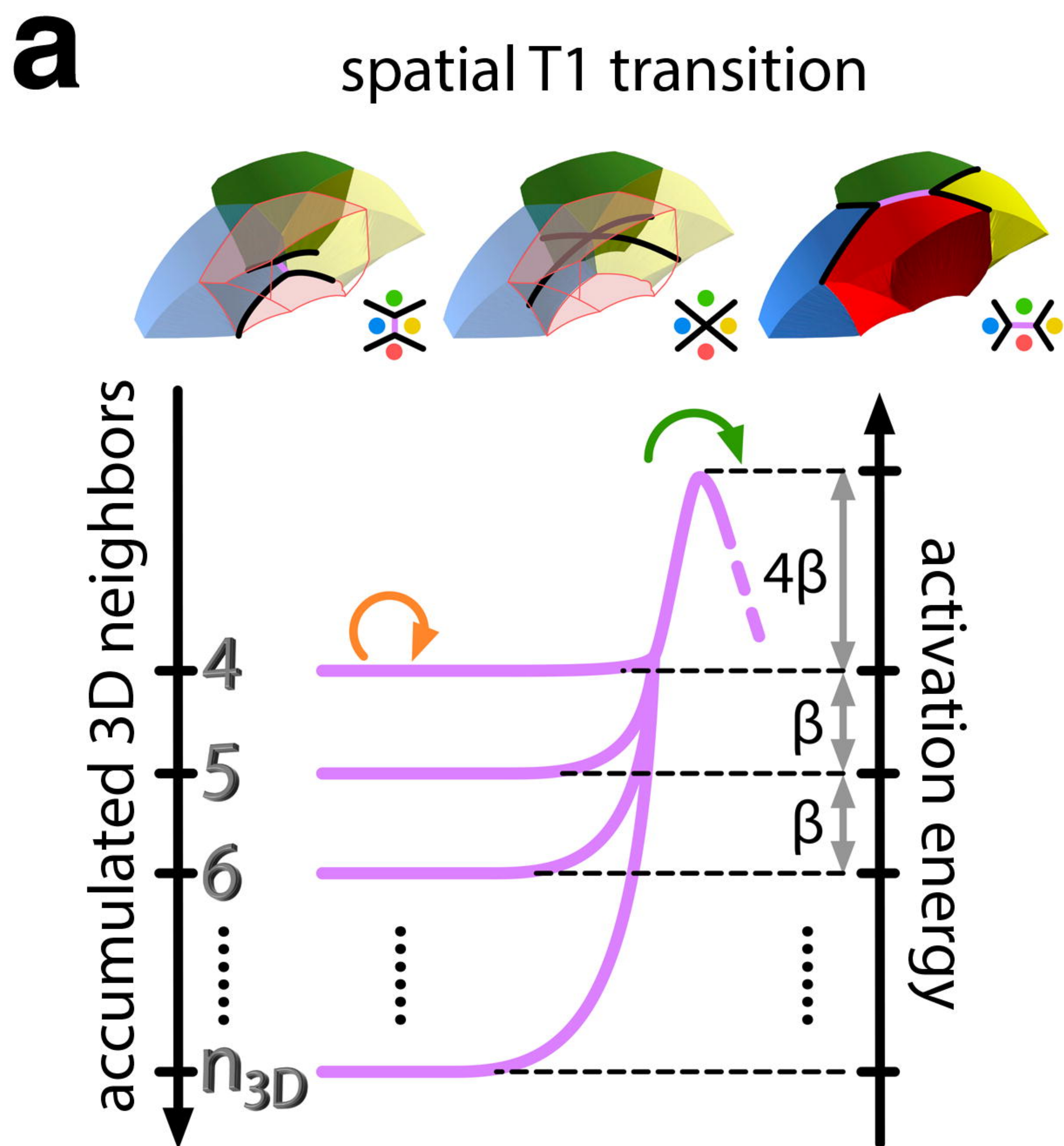


**a****b**

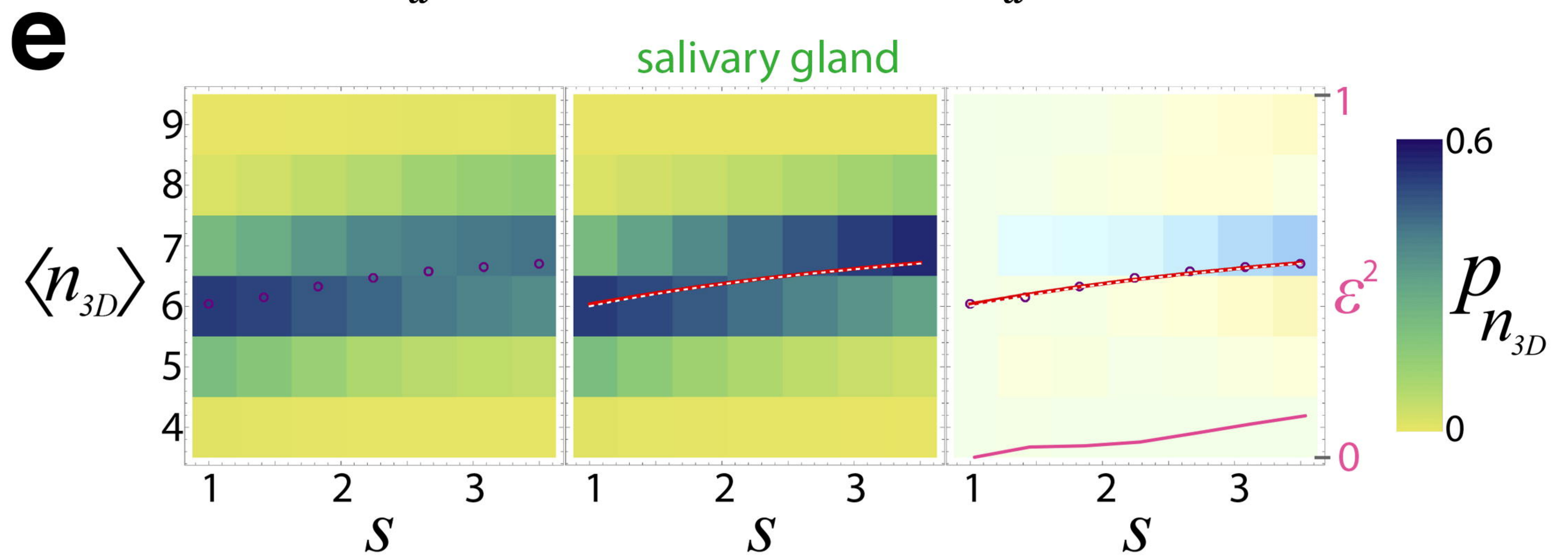
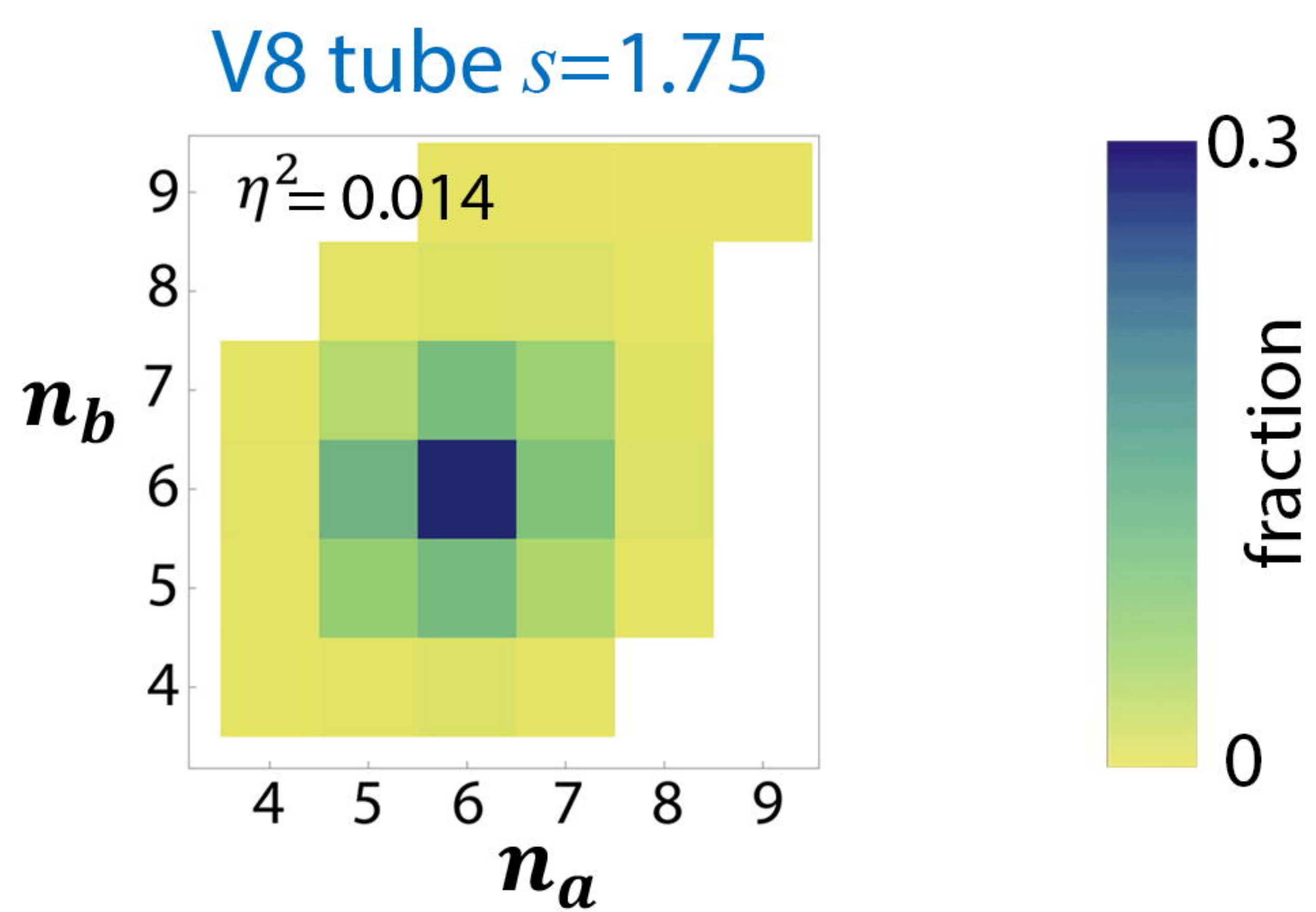
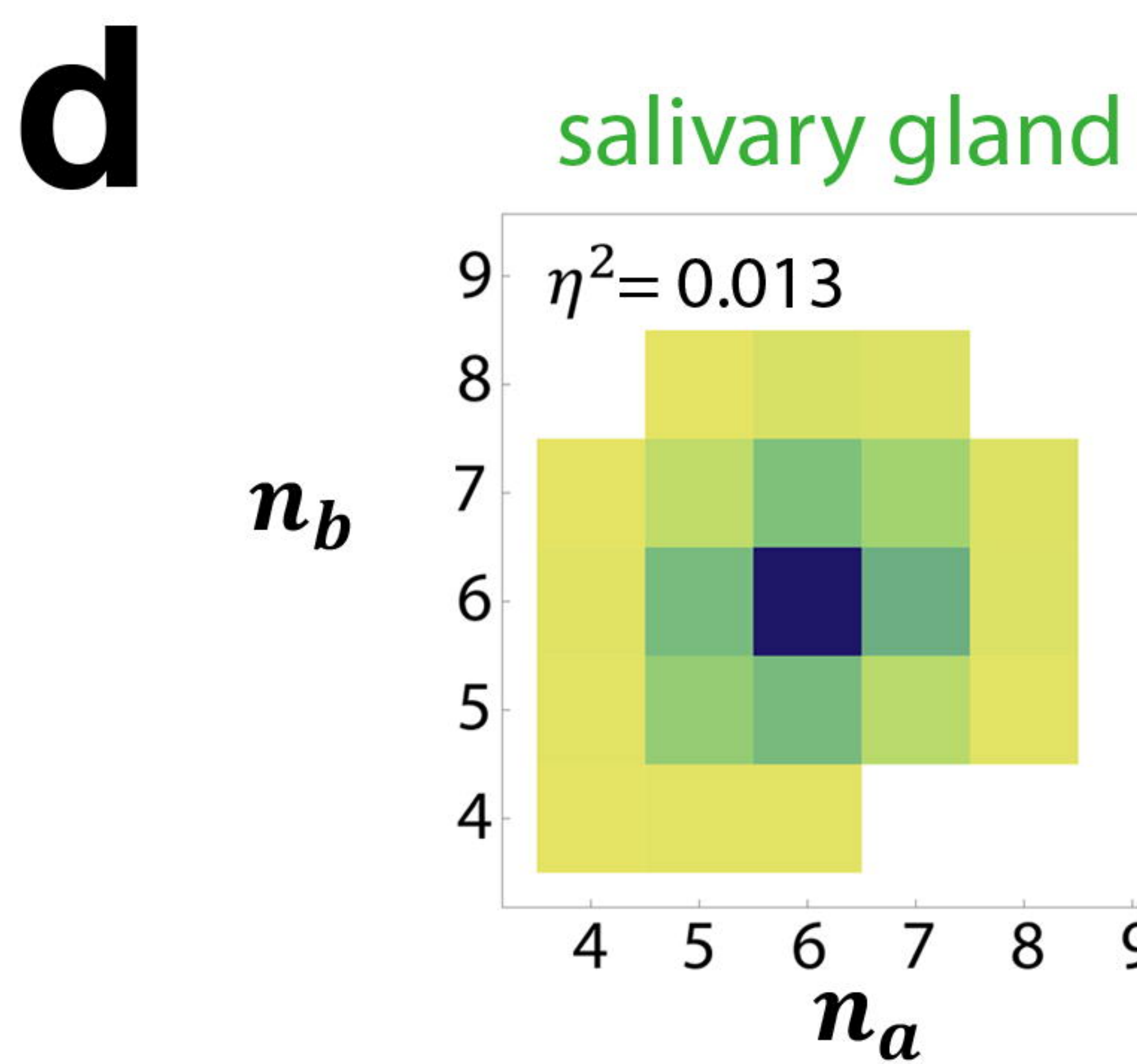
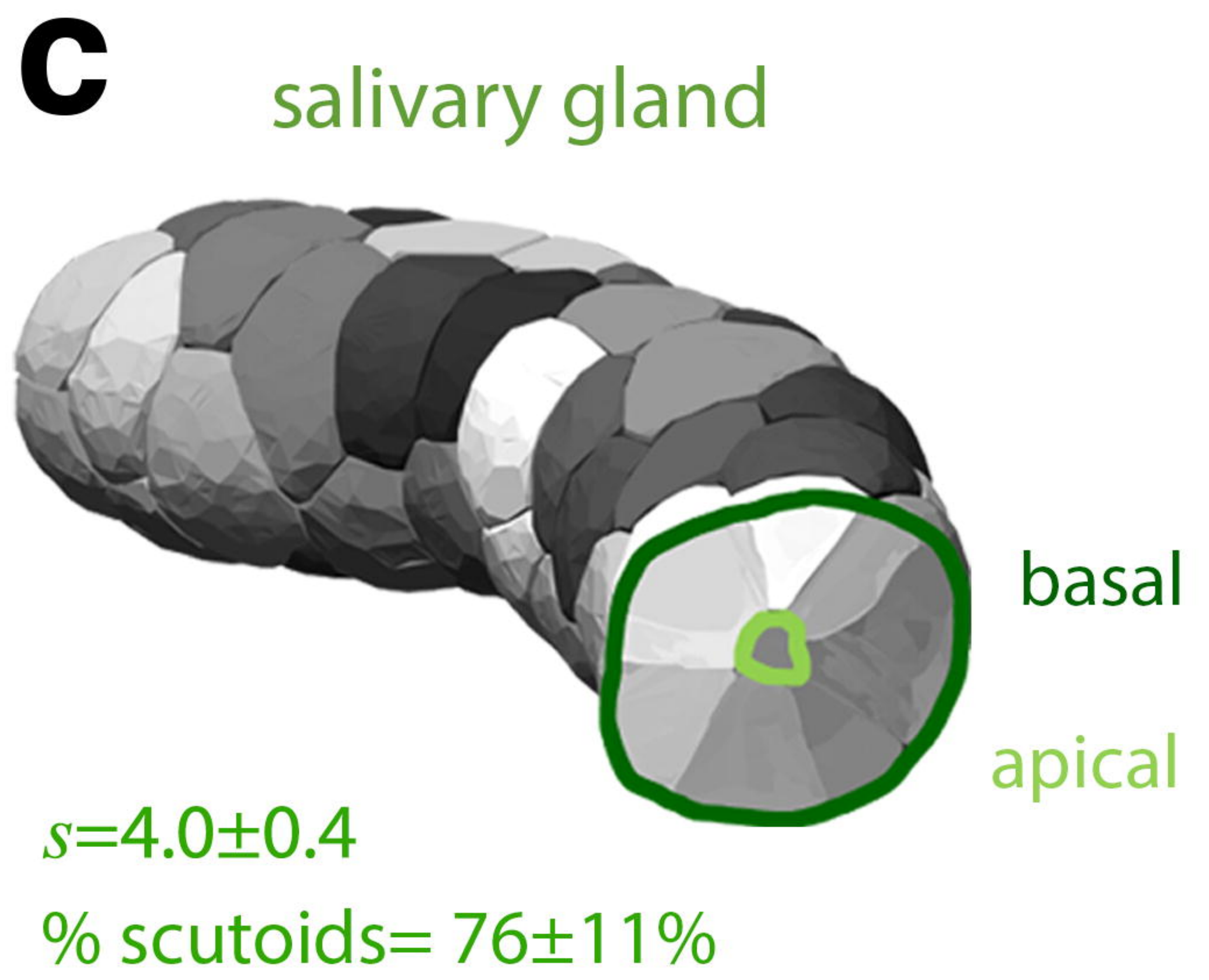
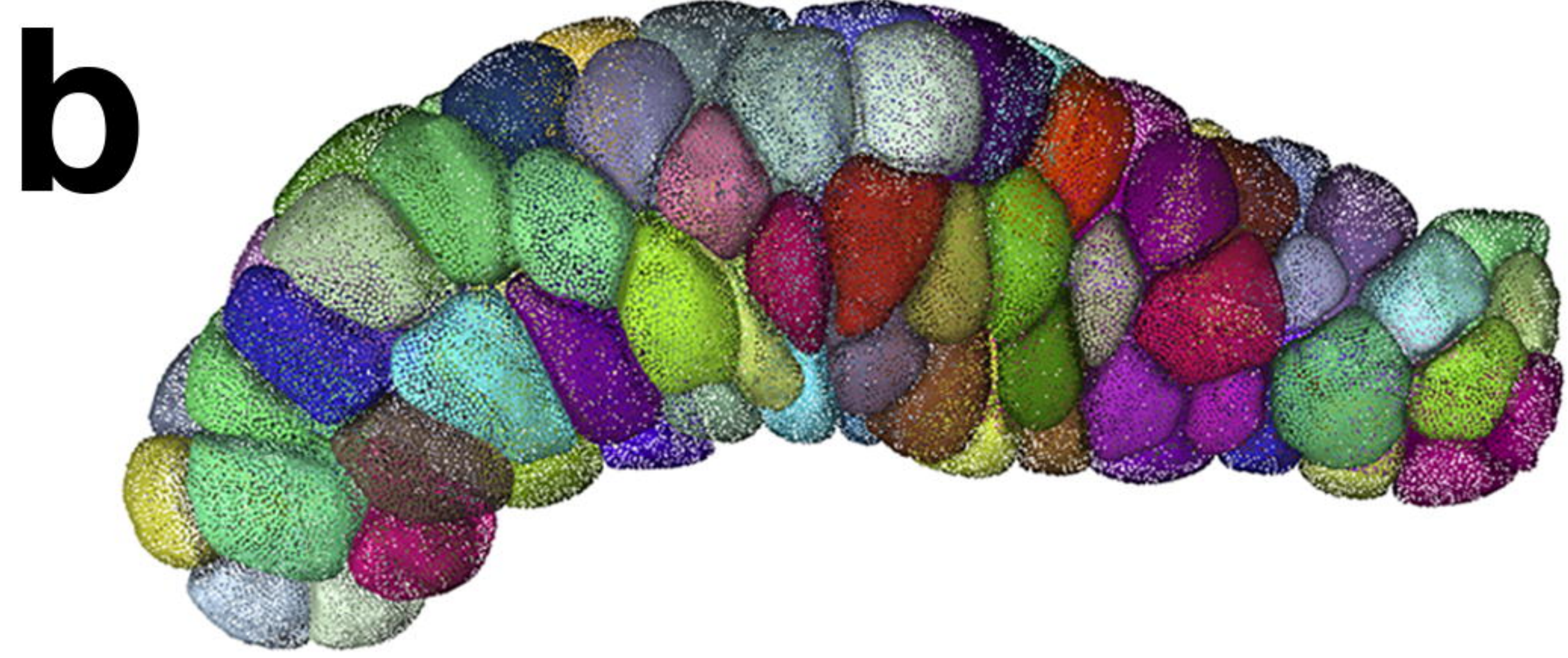
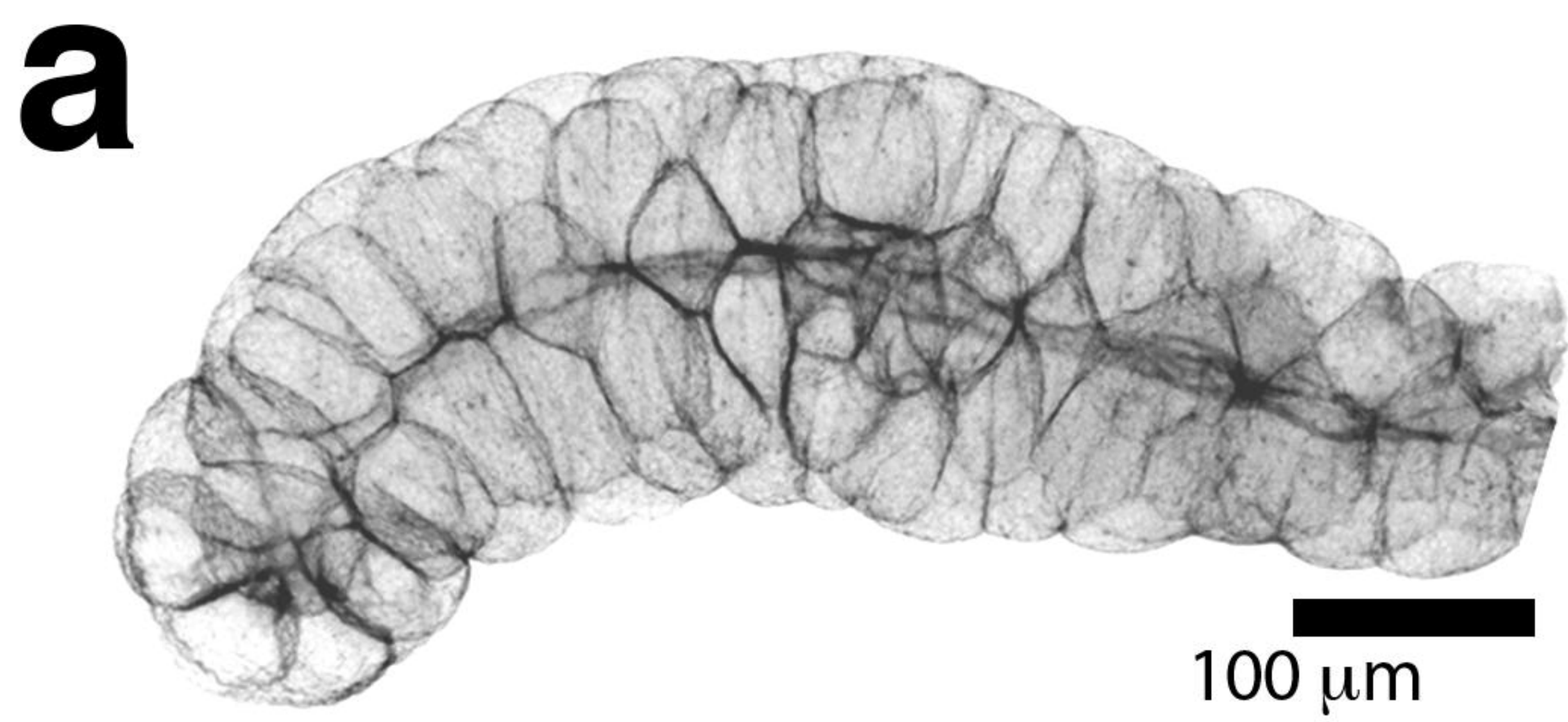












V8 tube

